Building 3D Dense Reconstructions using LiDAR Data

Marcelo Gennari do Nascimento

Wadham College, University of Oxford

May 2, 2018

Abstract

Autonomous mobile robots depend on three connected fields of Robotics: perception, planning and control. The perception problem tries to answer where the robot is in relation to its surroundings, and it is a crucial step in planning and control. In recent years, many algorithms have been developed that solve very specific perception problems, although loosely related to each other. Some of these algorithms include Visual Odometry, Laser Odometry, Simultaneous Localization and Mapping, and 3D Reconstruction Systems. A full working autonomous mobile robot will have to integrate all of these algorithms and methods to work as expected even in challenging situations. The purpose of this project is to put together many of the modern algorithms in perception to evaluate how an integrated system performs with real-life data. The full system presented here consists of state-of-the-art algorithms in the fields aforementioned. The system is put to test using two different real-world datasets collected using the MultiSense SL sensor. It is hoped that this project will give rise to more integrated systems and an insight on the areas that need to be explored and further developed for a fully autonomous system.

Contents

1 Introduction

Autonomous robots are going to be one of the major achievements of science to the benefit of the public. Autonomy though depends on two main problems that are closely related to each other: Localization and Mapping. The first concerns the problem of estimating the robot's position in an environment given a map as a prior. The second concerns the problem of mapping the environment given a prior robot's trajectory. Most of the time though, neither the trajectory nor the map is known *a priori*, and they need to be built simultaneously.

This is done by integrating a variety of sensors that can be categorized into proprioceptive or exteroceptive. Proprioceptive sensors provide data information about the robot itself, such as the forces in their joints and wheel encoders. Exteroceptive sensors give data information about the environment, using visual or laser scans for example. This is also called "observations".

Since the 1986 IEEE Robotics and Automation Conference, researchers have framed the general problem of Simultaneous Localization and Mapping (SLAM) as the "holy grail" of modern robotics [1]. A reliable solution to this problem would make autonomy one step closer to reality. Since the conference, a number of algorithms have been developed that successfully tackle SLAM, each with their advantages and drawbacks. By integrating proprioceptive (inertial and kinematic) and exteroceptive (i.e. LiDAR) sensors, modern methods of localization are able to predict the position of a walking robot to within 2cm [2].

In order to make the map built have significant meaning and be of use to people, it is necessary to reconstruct it in 3D (or volumetrically). A 3D reconstruction system would give geometric, semantic and graphical meaning to maps, which then can be used for augmented or virtual reality for exampled.

Volumetric reconstruction relies heavily on tracking the robot's position, since the observation accuracy is independent from other observations but bounded by the tracking accuracy. Therefore, by using modern techniques to solve the problem of SLAM, it would be possible to build a reliable and realistic map of an environment without any prior information about how the environment is structured. Obvious direct applications for such a system would be reconnaissance, search and rescue, and transportation.

1.1 Aim of the Project

This project is concerned about developing state-of-the-art algorithms for SLAM and reconstruction systems to reliably and efficiently build a 3D map of an environment with LiDAR data from a walking robot without any prior map or trajectory available. Since the robot is most likely to operate indoors and in situations where no off board sensor is available, it was decided to not use any wirelessly transmitted information, such as GPS (Global Positioning System) or Motion Capture Systems.

Many papers have been published on the individual building blocks that form the components of this project, whereas academic reports that put all of the state-of-the-art algorithms together to form a working system are much rarer. This report is the result of such a system. The contributions of this report are: (1) The design of a SLAM and 3D Reconstruction system integrating modern algorithms; (2) Validation of the system in real-data collected using a LiDAR sensor.

1.2 Organisation of the Report

Section 2 of the report will go through the literature review of the main building blocks of the project. In particular, current developments in the solutions of the Simultaneous Localization and Mapping (SLAM), Stereo Visual Odometry, the Iterative Closest Point Registration (ICP), and 3D Reconstruction problem.

Section 3 will go deeper on the system pipeline of the project. In order to get a general understanding of the system, detailed explanation of the steps of data processing, inputting and outputting will be explained. This will also introduce the two main parts of the system that will be explained in subsequent Section and analyse the tools used in the project.

Section 4 explores the solution of the SLAM problem adopted in the project. Since building an accurate map is an essential step to the success of the project, this Section will explain the details of how the SLAM solution works and why this particular structure was chosen.

Section 5 shows how the output from the SLAM solution will be integrated with the 3D reconstruction system. This has been a major topic of research in Computer Vision and Computer Graphics, but have mainly been tackled in small environments and in hand-held devices. In this Section, a solution for large scale reconstruction, and an overview of the parameters and trade-off involved in the process will be explored.

Section 6 presents the results on real-data, collected using LiDAR sensors. In this Section, the software and hardware used to get the results, and a comparison between the results in the datasets will also be presented.

Section 7 will conclude the report with an overall evaluation of how the system performed. It will also indicate ways in which the system could be improved in a subsequent project. An analysis of how the outcome of this project compares with similar systems will be provided.

2 Literature Review

In order to have a complete overview of the system, it is important to review both the hardware and software used in this project. The possible choices for sensors and the situations in which they are suitable will be explained next. Then the necessary algorithms for SLAM and 3D reconstruction will be briefly reviewed.

2.1 Range Sensors

Range Sensors are devices used to get depth information using a variety of methods. An overview of the main mobile active sensors will be considered. There are three main types of sensors: time-of-flight sensors, structured light sensors, and stereo cameras.

2.1.1 Stereo Cameras

Stereo Cameras are passive sensors (sensors that do not have their own light source) which use the difference in position of two cameras to convey depth. This is analogous to how most mammals see and one of the reasons why humans can perceive depth (humans also use monocular cues [3]).

An advantage of Stereo Cameras is that they are energy efficient since they are passive systems and they work well when there is natural illumination (outdoors for example). They are also a technology that has been extensively studied and sold by a plethora of companies.

Some of the most limiting factors in the use of Stereo Cameras is that they need to solve the correspondence problem to get depth information, which depends on the extraction of features (see Section 2.3). This is computationally inefficient as it requires algorithmically complex systems to extract features. Consequently, such systems can only solve the correspondence problem in situations where there is sufficient texture in the scene (plenty of edges and corners for example). Consider a white wall for instance: since there are not much features that could be extracted, the correspondence would be unreliable and render a poor estimation of depth for the stereo vision. This limitation is not faced by Active Sensors (sensors that have their own light source) for example.

2.1.2 Structured Light Sensors

Structured Light Sensors have become particularly popular since the release of the Kinect Sensor by Microsoft [4](see Figure 1). It works by projecting a pattern of infra-red light, sensing the reflected light and producing a disparity map. It is analogous to a stereo camera where one of the cameras is replaced by a light emitter. The advantages of using this method instead of pure stereo vision for depth information is that it works well in low light situations, it requires less computation meaning that it can be operated at higher frame rates, and it can produce a result independently of the texture available in the scene.

Figure 1: Microsoft's Kinect Sensor, which uses structured light to get depth information. The arrows indicate the positions of the projector, the RGB camera and the Infrared camera (marked as IR). Figure taken from Sarbolandi et al. [5]

One disadvantage of using this method is that since it emits its own light, it has a limit on how illuminated the scene can be. It works in the dark (which is not true for stereo cameras), but in highly illuminated scenes, there is a lot of interference from sunlight. It also doesn't work well with specular surfaces, which do not reflect light back to the sensor unless the camera is positioned in an appropriate orientation i.e. in the path of the reflected beam.

2.1.3 Time of Flight Sensors

Time of Flight Sensors work by projecting a laser beam at an object, detecting the reflected beam using a photodiode and calculating the time interval to calculate an estimate of range [6]. The time between projection and reflection can be measured using the phase difference of the projected and incident beam. A more detailed explanation can be found at [6].

These sensors can be further divided in two different categories: scan and scannerless sensors. Scan sensors work by projecting a fine laser beam alongside a rotating mirror to obtain a planar scan. The 3D information is then obtained by further rotating the mirror about another orthogonal axis concurrently. This is how LiDAR sensors work ([6]). Scannerless sensors can also

be implemented by diverging the beam from one single source to produce an array of information detected by an array of photodiodes. This is how modern depth cameras work, including the new KinectV2 depth camera [7].

2.1.4 Comparison of Sensors

In order to overview how different sensor technologies work, Table 1 is provided. It contains a summary of the main capabilities of the most well known sensors in each category. As specifications of different devices widely vary even when using the same technology, one device for each category was picked as being representative of how each technology performs in general.

	ToF Camera (Kinect v2)	**ToF LiDAR** (Houkyo UTM-30LX-EW)	**Structured Light** (Kinect v1)	**Stereo Camera** (Bumblebee)
Robust To Daylight	Variant	Yes	No	Yes
Robust To Low Light Conditions	Yes	Yes	Yes	No
Range	Scalable	0.1m-30m	0.4m-8m	0.5m-4.5m
Bandwidth (Points per sec)	65 000 000	43 000	9 126 000	160 000 000

Table 1: Overview of main differences in different Depth Sensor Technologies. The word "Variant" means that different devices might experience different properties. In each of the categories, a sample device was taken as reference (shown in parenthesis). However different devices may exhibit varying properties. The values were calculated using [7], [8], [9], [10], [11].

The Bandwidth in Table 1 was calculated by multiplying the resolution of each frame (pixel x pixel) by the number of frames per second. This way, we can get an upper limit on the number of points generated every second. It is known that many of these pixels end up not containing any depth data at all, especially when there are many specular materials in the scene. However, this is the best way of comparing different technologies without having to do an in-depth analysis of each of them.

2.1.5 Multimodal Sensors

There are plenty of options for coupling different the sensors together to optimise the overall performance. The main sensor used in this report is the MultiSense SL by Carnegie

Mellon Technologies [10] (see Figure 2).

Figure 2: Carnegie Mellon Technology's MultiSense SL tri-modal Sensor. On the bottom of the sensor the stereo camera can be seen. A Hokuyo UTM-30LX-EW laser scan is attached in a rotating device. The sensor also outputs video in a high-data-rate. Figure and reference from [12]

This sensor is a tri-modal sensor, which integrates a LiDAR scanner, a Stereo Camera, and a Video stream. In Section 6, the results of using this sensor in two different datasets are shown.

2.2 Simultaneous Localization and Mapping (SLAM)

SLAM is the problem of whether it is possible for a mobile robot to create a globally consistent map of an environment and localize itself on it without prior knowledge of the map [1][13]. Building a map of an environment is a crucial step towards autonomy, since planning and control assume prior knowledge of mapping and localization. Mathematically, we can frame SLAM as a Bayes Net. Defining:

- $\mathbf{x_k}$: the pose of the robot (being $\mathbf{X_{0:k}}$ as the poses from time $\mathbf{0}$ to $\mathbf{k}$)
- $\mathbf{u_k}$: the odometry measurement ($\mathbf{U_{0:k}}$ as the historical measurements)
- $\mathbf{l_k}$: the landmark position ($\mathbf{L_{0:k}}$ as the historical landmarks)
- $\mathbf{z_k}$: the landmark observation ($\mathbf{Z_{0:k}}$ as the historical landmarks)
- $\mathbf{c_k}$: the loop closures

It is possible to formulate the problem of SLAM more formally using the following graphical model:

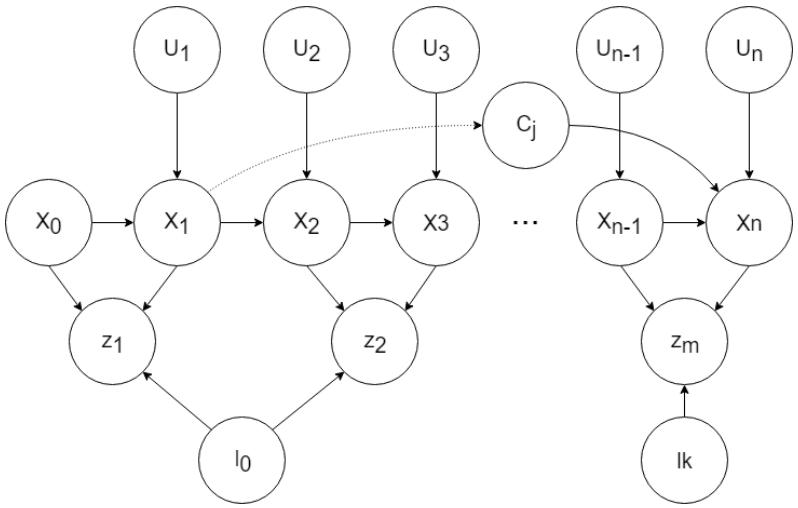

Figure 3: SLAM as a Bayes Net. The value $\mathbf{x_0}$ denotes a prior; $\mathbf{x_n}$ denotes the state vector; $\mathbf{u_n}$ denotes odometry measurements; $\mathbf{c}$ denotes close loops; $\mathbf{l_n}$ denotes landmark positions.

The graph shown in Figure 3 is a Bayes Network representation of the dependencies between variables. A probabilistic framework can then be extracted from it.

$$P(X, L, U, Z) \;\propto\; P(x_0) \prod_{j=1}^{M} P(x_j | x_{j-c}, c_j) \prod_{i=1}^{M} P(x_i | x_{i-1}, u_i) \prod_{k=1}^{K} P(z_k | x_{i_k}, l_{j_k}) \tag{1}$$

The general goal of probabilistic SLAM is to find variables $\mathbf{X}^*$ and $\mathbf{L}^*$ that maximizes the posterior probability distribution $P(X, L \mid U, Z)$ of the Equation 1. Two models of the probabilities given above are used commonly in SLAM to tackle this problem: the Process Model (also known as Motion Model in mobile robotics) and Observation Model:

Process Model :

$$x_i = f(x_{i-1}, u_i) + w_i$$

Observation Model :

$$z_i = h(x_{i_k}, l_{j_k}) + v_k$$

Where w_i is white noise with covariance Q and v_k is white noise with covariance R. The process (motion) model is usually a generalization of how the robot moves (kinematics) [14][15]. The observation model is a probabilistic representation of the performance of the sensors used to collect the data. Notice that both models are probabilistic and thus define the probability distributions $p(x_i|x_{i-1}, u_i)$ and $p(z_k|x_{i_k}, l_{j_k})$.

Under this framework, it was shown that the SLAM problem is indeed feasible, and that it builds a nondivergent map with no prior information [16]. So it is widely accepted that in theoretical grounds, SLAM is a solved problem [1][13][16][17]. However, there are computational

and algorithmic challenges that hinders the development of a real-time implementation system that performs SLAM. This problem gets even more complicated when considering unstructured environments and large scale maps [18].

There are three main implementations of SLAM: Kalman Filtering and Extended Kalman Filtering (with early works such as proposed by R. Smith [19]), Particle Filtering (most notably with FastSLAM [14]) and Least Squares Graph (with iSAM from Michael Kaess [20]).

2.2.1 Kalman Filtering

As one of the first implementations to attempt to solve the problem of SLAM, the Extended Kalman Filtering (EKF) approach makes two approximations when formulating the probabilistic SLAM: both the Process Model and the Observation Model are linearised about a suitable linearisation point $\hat{x}$.

Subsequently, the probability distributions $p(x_i|x_{i-1}, u_i)$ and $p(z_i|x_i, l_i)$ are modelled as Gaussians with the means $\nabla f|_{x=\hat{x}}$ and $\nabla h|_{x=\hat{x}}$ and covariances Q and R. With this framework in place, a recursive two-step method can be found to update the posterior probability distribution at every iteration [1]:

$$\textbf{Prediction Phase}: \; P(x_i, L|Z_{0:i-1}, U_{0:i}) = \int P(x_i|x_{i-1}, u_i)P(x_{i-1}, L|Z_{0:i-1}, U_{0:i-1})dx_{i-1}$$

$$\textbf{Update Phase}: \; P(x_i, L|Z, U) = \frac{P(x_i, L|Z_{i-1}, U)P(z_i|x_i, L)}{P(z_i|Z, U)}$$

The Prediction Phase concerns the motion model, where an update of the estimated position of the mobile robot is made taking into account only the controls and kinematics of the robot itself. This is followed by an Update Phase, where the position of the robot is recalculated based on the observation of a landmark, for example. This algorithm is then recursively applied for every time-step i.

Since the product of two Gaussians is a Gaussian, the probability density function $p(x_i, L|Z, U)$ will remain Gaussian at all times, and a closed loop solution using just the mean

and the covariance matrices can be found [15].

Analysis of the EKF algorithms have shown that due to linearisation of the functions f and h, assumptions about Gaussian Process and Observation Model can cause the EKF solution to perform poorly unless many loop closures are detected in frequent intervals [21].

It is also known that the Kalman Filter approach requires storage of the order of $O(N^2)$ (where N is the number of features), and for a classic implementation of the algorithm, it also requires computational power of the order of $O(N^2)$ [16]. New methods for computing the covariances (which cause the squared dependence) by exploring state augmentation, partitioned updates and sparsity in the matrices have demonstrated faster solutions, thus requiring less computational power [18].

2.2.2 Particle Filtering

In order to avoid linearisation of non-linear models, Particle Filtering (PF) has been a popular method to integrate non-Gaussian distributions in the estimation [14][15]. The basis of particle filtering comes from Dellaert's proposal of a Monte Carlo Localization (MCL) algorithm [15]. In sampling methods, the probability distributions are defined as a function of the density of particles along the distribution. This approach avoids the assumption of linearity and Gaussian distribution, which makes this algorithm embrace multi-modal distributions.

Just like the EKF solution, there are many different implementations of PF methods. However, most of them follow the basic structure of the FastSLAM algorithm [14]. This algorithm breaks the SLAM problem in one of localization over the robot's path, and k landmark location, where k is the number of landmarks. The Localization problem is solved using MCL, which is composed of two parts [15]:

Prediction Phase: In this part, N number of particles are drawn from the Motion Model distribution, whose density asymptotically represents the proposal distribution $P(X, L|Z_{0:i-1}, U)$.

Update Phase: Each particle from the Prediction Phase is then given a weight which is equal to the likelihood of the particle being there given the observation. In other words, $weight =$

$P(Z|X, L)$, which is drawn from the Observation Model.

After those two phases, the Landmark Location is solved using the classical EKF algorithm.

Particle filtering methods have advantages over the EKF for not making any assumptions about linearity or Gaussianity of the distribution. Also if implemented wisely, it can reach $O(Mlog(K))$ time, where M is the number of particles and K is the number of landmarks [14].

2.2.3 Least Squares Graph

This is particularly applied to iSAM [20]. The biggest difference of this approach is that instead of marginalizing out poses and working with the current position (which is done in any Filtering approach), iSAM uses a Smoothing approach, which takes into account all of the past poses of the graph.

This seems more computationally expensive than marginalizing out many poses, but usually the Information Matrix using this approach is considerably sparse, which accelerates the computation of the inverse using QR decomposition

At the end, iSAM works by linearising the system and solving the linear problem $Ax = B$, where x is the augmented vector state that contains all of the poses and the landmark positions.

When linearising the system though, using iSAM approach, the linearisation point does not need to be fixed in time. So at every iteration, a new linearisation point is computed, which means that over time no information is lost.

Then by using a simple QR decomposition the system can be solved in real time. The only concern is that loop closures add a significant amount of density in the Information Matrix, which means that the computation of the linear equation cannot be computed very quickly.

This is solved by using a technique called "rearranging coefficients", which is an NP problem but fortunately has algorithmic solutions that can find good approximations of the optimum solution in real time.

This was the system chose to run the experiments in this report for being fast, have support for pose-only graphs and being open source, support for C++ and providing all the tools necessary for the purpose of this project.

2.3 Stereo Visual Odometry

Visual Odometry concerns the problem of estimating the robot's pose using its camera sensors. When two calibrated cameras are used, it is called Stereo Visual Odometry. It is a useful estimation procedure that can substitute wheel odometry in cases it is not available or it is not accurate (e.g. in rough terrain where the wheels slip).

The standard Stereo Visual Odometry algorithm works as follows [22]:

1. Preprocessing Images: rectify images so that epipolar lines are aligned in left/right images; smooth images with an edge preserving filter such as the bilateral filter; calculate disparity map, by Block Sum of Absolute Difference (SAD) or equivalent, which indicates the inverse range map.
2. Detect Features: use either Harris [23], FAST [24] or SIFT [25] for example, to extract features in the images.
3. Match Features: by using a Score Matrix from the disparity map.
4. Estimate Motion: by means of re-projection and triangulation of the calibrated cameras.

Stereo Visual Odometry is relatively accurate when cameras are properly calibrated, and results of the order of 0.25% accuracy over 400m have been achieved using only the pure algorithm [22]. The tool used in this project was FOVIS (Fast Odometry from Vision) [26], which is described in [27].

2.4 Iterative Closest Points (ICP)

The problem that ICP is trying to solve is as follows: given a point cloud in a sensor coordinate frame that is a subset of a complex shape of another point cloud in a model coordinate

frame, what is the translation and the rotation that aligns, or registers, the clouds by finding the minimum of a distance metric?

Given a point cloud in the sensor reference frame $P = \{p_1, p_2, p_3 ... p_{N_p}\}$, which is a subset of the point cloud in the model reference frame $X = \{x_1, x_2, x_3, ... x_{N_x}\}$, and assuming that the correspondence P to X is known and is $C = \{(x_1, p_1), (x_2, p_2), ..., (x_N, p_N)\}$, the minimum square error be formulated with the following equation:

$$f(\overrightarrow{q}) = f(\mathbf{R}, \overrightarrow{q_t}) = \frac{1}{N} \sum_{i=1}^{N} ||\overrightarrow{x_i} - \mathbf{R}(\overrightarrow{q_R})\overrightarrow{p_i} - \overrightarrow{q_t}||^2 \tag{2}$$

Equation 2 is a function of the Rotation Matrix $\mathbf{R}$ and the translation vector $\overrightarrow{q_t}$. It is computationally cheaper to define the Rotation Matrix as a function of the quaternion q_R, as it only requires 4 variables instead of the 6 needed for the full Rotation Matrix. If we define the vector $\overrightarrow{q} = [\overrightarrow{q_R}|\overrightarrow{q_t}]^T$, then we can optimize the above as a function of the 7 variable vector $\overrightarrow{q}$ [28]. This vector would then define a translation from P to X that would minimize the objective function.

Using that equation, a simple ICP algorithm can be implemented using the following iterative operation:

1. Find the correspondences between points X and P by evaluating closest points in each of the points of the smallest set. This correspondence can be efficiently calculated using for example KD-Trees, Octrees, or other variants [29].

2. Compute the registration by finding $\underset{\overrightarrow{q*}}{min} f(\overrightarrow{q})$ and apply the transformation to the whole set P. This can efficiently be calculated by using QR Decomposition or Singular Value Decomposition [30].

3. If $f(\overrightarrow{q*}) \leq \tau$, where τ is a threshold value, then stop. Otherwise go back to step 1.

The ICP algorithm formulated with the above objective function always converges monotonically to the nearest local minimum [28]. The global minimum is more difficult to find, since it depends on the relative initial pose of the model and the sensor reference frames. Thus, the global minimum will only be found when an adequate initial pose is given, which usually

means that the initial pose is close to the reference pose [28].

Since first formulated, a number of variants of the ICP appeared. They are usually alternative ways of selecting subsets of the points, finding correspondences, weighting correspondences, rejecting specific pairs, assigning an error metric, computing the minimum of the objective function, or a combination of these [30]. The variant used in the project was the AICP, which rejects point correspondences based on the overlap between point clouds [31].

2.5 3D Reconstruction Systems

Although point clouds can be very useful for tasks such as correction of poses, they do not provide for higher level of scene understanding. 3D Reconstruction Systems are used for that: given discrete data from a sensor, the 3D Reconstruction System tries to recreate the scene geometrically by estimating surfaces and occupancy, and graphically by providing texture.

In order to represent surfaces, there have been a couple of algorithms that have been used. The most popular one uses the idea of Signed Distance Functions (SDF), which is a scalar function that represents distances to the nearest surface. Given known poses and range data, the world is modelled as a voxel grid in which each voxel holds a value that represents its distance from the closest surface. Positive numbers mean that the voxel is in front of the surface and negative values means that the voxel is behind the surface. The voxel grid then represents isosurfaces at the zero crossing which can be extracted in polygon meshes using an algorithm such as the Marching Cubes [32].

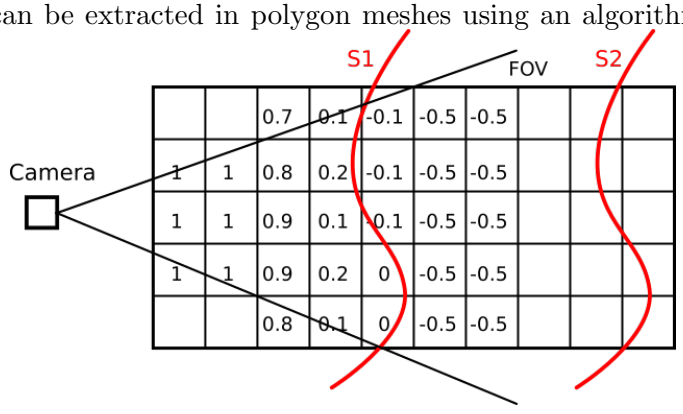

Figure 4: Graphical representation of a voxel grid. Each Grid has a Truncated Signed Distance Function value corresponding to the distance to the nearest surface. In order to avoid interfering with other surfaces, the value assignment to voxels that are far away are taped off after a few voxels

This method of characterizing reconstruction is very useful for a number of reasons. One can think that given a point cloud, using triangulation (such as Delaunay Triangulation), surfaces would be generated. The problem with simple triangulation methods is that they do not account for noise when collecting range

data, and they are harder to incrementally fuse different sets of data. By using weights on each voxel, it was shown in [33] that many scans can be integrated by simply summing the values of the voxels weighted by their respective weight according to a specified weighting function. This makes it easier to integrate different scans and different types of data (for example, Point Clouds and RGBD data), as well as uncertainty based on the defined weight functions of each sensor. Other methods used when adopting this scheme include the concept of the Truncated Signed Distance Function (TSDF [33]), in which the weighting values are tapered off behind the surfaces to avoid interference with other surfaces (see Figure 4).

There are mainly three classes of reconstruction systems that can be found in the literature:

- Active vs Passive Sensors: when using an active sensor (such as Kinect to get RGB-D images), the depth estimates are accurate enough so that a simple fusion using weights is sufficient to extract an appropriate reconstruction (example system KinectFusion [4]); when using a passive sensor (such as in DTAM [34]), the depth estimates are usually less accurate and thus there is a need to use a regularizer.

- Object-Centric vs Mobile-Robot-Centric Fusion: when in object-centric situation, it can be assumed that the voxel block and the voxel grid will be seen all of the time by the sensors (such as in KinectFusion [4]). Also, the object is seen in loops multiple times, thus allowing for fine detailed reconstructions; this is not true for a mobile-robot-centric situation, where the robot navigates through the scene instead of around it, and new voxel blocks have to be dynamically allocated depending on the robot's trajectory (such as in Kintinuous [35], even though it still uses fixed voxel blocks). It is also unlikely that the same scene is going to be seen multiple times in a range of different angles. The difference between the two modes is best illustrate in Figure 5, taken from [36], which shows the two different modes of fusion based on the movement of the sensor.

- Large vs Small Scale: memory allocation plays a huge part when large scale models are used, and that comes at a cost of usually higher voxel sizes, whereas in small scale very small voxel sizes and details can be preserved. Examples of systems that took memory in consideration include the Hashing Voxel Grid (HVG) approach in [37]

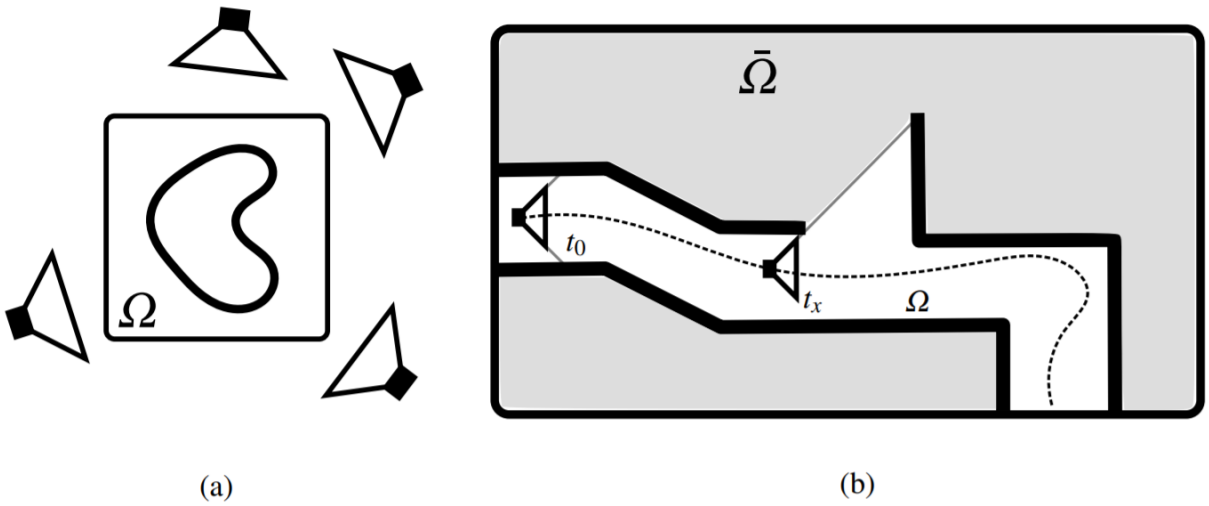

Figure 5: Image taken from [36]. It shows the two ways of reconstructing a system based on the movement of the sensor. (a) indicates the Object-Centric Fusion and (b) indicates the Mobile-Robot-Centric Fusion. It can be seen that whereas in (a) the scene Ω is seen at all times, in (b) there are seen scenes Ω and unseen ones $\overline{\Omega}$ that change with time.

Due to the RGB-D sensor becoming widely available as a commodity (as shown in [4]), most 3D reconstruction systems have focused on hand-held devices for small scale reconstruction. Since this project relies on LiDAR data for large scale reconstruction, a new system has been chosen.

The system used in this report is BORG-CUBES: a reconstruction system that uses sensor-agnostic voxel grids to reconstruct the environment. As described in [36], because LiDAR data come at lower frequency than RGB-D data, BORG-CUBES relies on a prior regularizer to improve the quality of the reconstruction. Specifically, it uses the Total Variation (TV) regularizer, which penalizes high varying surfaces with the assumption that noisy signals have high total variations. More details of this approach are explained in Section 5, or can be read in the original paper in [36]. It can also integrate stereo visual images, which gives data in higher rates but provide a much lower quality depth map than using LiDAR or RGBD data.

3 System Pipeline

The pipeline for the overall system can be seen below. It consists of 4 modules: (I) First odometry estimates; (II) Laser odometry; (III) Loop closure detection and Graph optimization; (IV) 3D dense volumetric reconstruction.

These 4 modules are broken down in two parts: the first part is concerned with solving the SLAM problem, which outputs a reliable trajectory and map. The second part is concerned with inputting that to a 3D reconstruction system to build the environment volumetrically. Figure 6 shows the overall system.

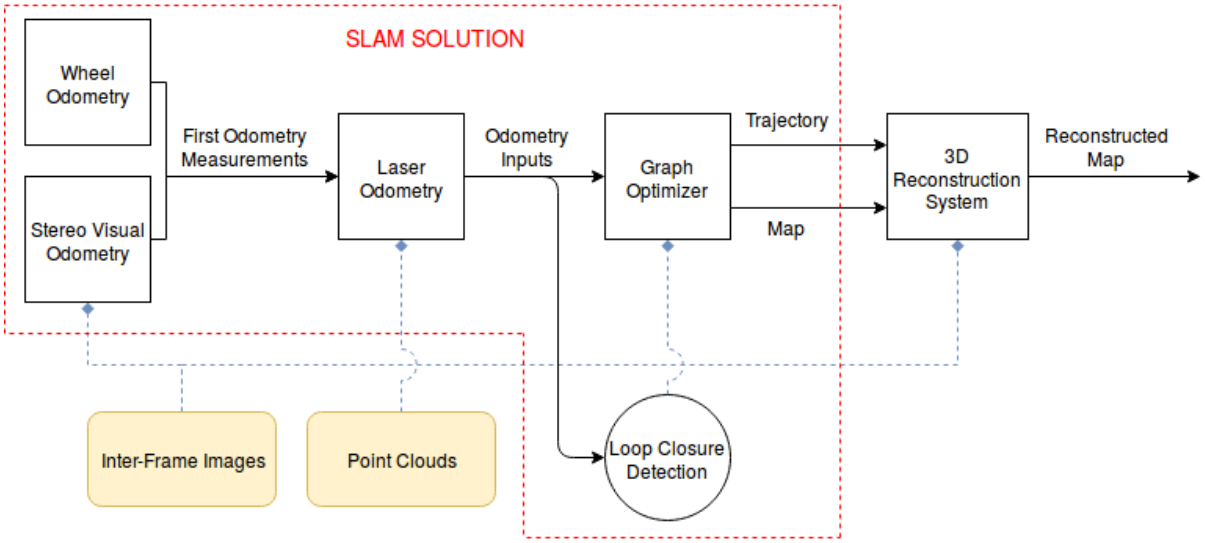

Figure 6: Diagram of the overall system pipeline. The beige boxes represent data collected from a sensor, the white boxes represent data being processed and the output being input to the next box. The rounded box is a module built for data association.

This pipeline is flexible enough so that many algorithms could be used for each of the modules described above. After consideration about the application of the system - keeping in mind the goal of implementing it in a mobile robot that reconstructs indoor scenes using LiDAR scans - the algorithms were chosen.

For the Visual Odometry, the FOVIS library [26] was used, as it is an open source library that has integration with C++ and works with 3D stereo data, which is used in one of the tests as described in Section 6.

For the Laser Odometry, the algorithm chosen was AICP [31], which works by correcting the odometry measurements by using the ICP algorithm every time a point cloud is

available. Since odometry measurements have a significantly higher data rate than the LiDAR sensors, an algorithm that corrects the poses incrementally given the laser scans was needed, and the AICP suits this requirement. Further details are going to be explained in Section 4.2.

For the graph optimizer, an algorithm that could take into account pose-only SLAM solutions was needed. A full explanation for this is postponed and explained in Section 4.4. The library used was iSAM [20], which is an open source library with support to C++, which can solve the problem of pose-only SLAM.

Since the system is going to be used only indoors and many loop closures are expected in a relatively short amount of time, a simple loop closure was implemented from scratch, which takes into account heuristics such as Euclidean Distance to match closures. The details of this choice is further explained in Section 4.3.

The 3D Reconstruction system needs to be able to reconstruct large-scale scenarios. It would be ideal as well to integrate different types of data, since the sensors used in the project allow for stereo and LiDAR data to be available. The framework used then was the BOR^{2}G-CUBES [36][38], which is sensor agnostic and implements a regularization term based on Total Variation algorithms to account for non-smooth surfaces. Further details of this implementation is shown in Section 5.

4 SLAM Solution

As already introduced in Section 3, the SLAM solution has 4 independent building blocks. This offers sufficient flexibility to test the effect that each part has on the outcome of the map. This section will discuss in more depth how the solution works with all the building blocks working together.

4.1 First Odometry Measurements

The first odometry measurements offer a relatively inaccurate estimation of the pose of the robot at a certain time. That is because they use methods that are less accurate when compared to laser scans, like stereo vision and wheel odometry (as demonstrated in [39] for example in the context of Micro Aerial Vehicles). The purpose of these first estimates is to give an input pose to the Laser Odometry algorithm to perform a better estimate of the trajectory. As shown in Equation 2, the ICP algorithm requires the initial pose of the reference frame of the two point clouds, denoted X and P in Section 2.4, and those are the poses that the first odometry measurements are supposed to provide.

Depending on how accurate those poses are, the ICP algorithm can find a global minimum (or get close to it) and offer a fine-tuned estimate of the trajectory. It is important then to get the first odometry measurements as accurate as possible, so that the Laser Odometry can always find a global minimum and make the trajectory optimum.

During the project, two methods to get the first odometry measurements were used. When collecting data with the mobile robot Husky [40], as shown in the "Edinburgh Dataset" introduced in Section 6, the wheel odometry provided by the system served as a good first estimate of its position. When getting the data with the MultiSense SL [10] for the "IEB Dataset" shown in Section 6, Stereo Visual Odometry from MultiSense's stereo camera was performed to get the first odometry estimations.

Stereo Visual Odometry

The Stereo Visual Odometry used is based on the system described at [27] and implemented with the FOVIS library [26]. Figure 7 shows one frame of the result of the visual odometry system when applied to the dataset collected for this project, referred to as the "IEB Dataset" in Section 6. The inputs came from the stereo camera in the MultiSense SL, collected at 30Hz in a relatively well illuminated indoors scenario.

There are a couple of important details that have to be taken into account when implementing the Stereo Visual Odometry. First, an important parameter when using Visual Odometry is the capture time. Since the system has to identify features (corners for example) very efficiently, considerably dark or light streams of images might make this job difficult.

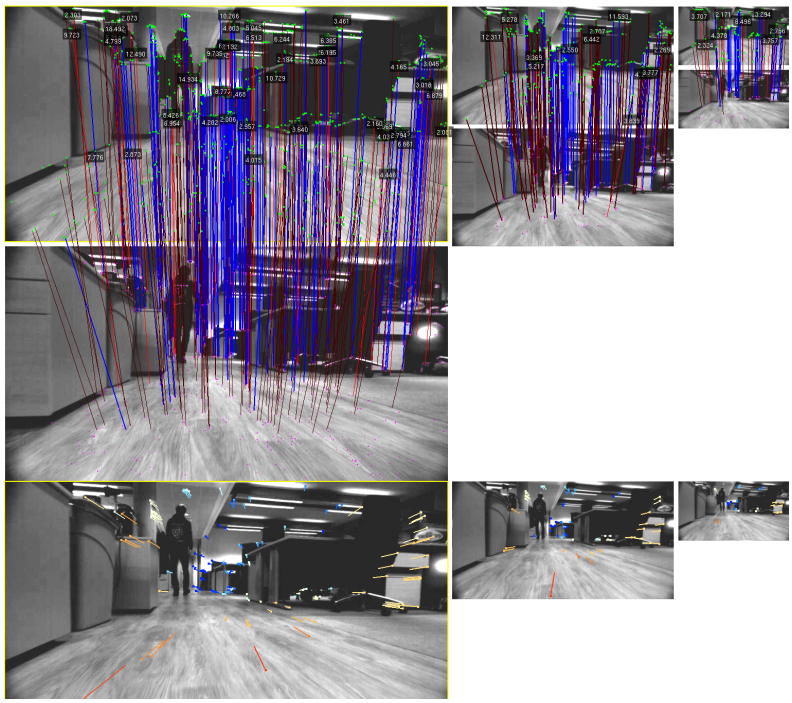

Figure 7: Result of FOVIS library to the data collected at the Information Engineering Building at University of Oxford. The first row of images show a Gaussian Pyramid to extract point features. The Key Frame is shown in the second row where features extracted are matched back to the first row images. Red lines indicate outliers and blue lines indicate inliers (bad and good correspondence respectively). The last row shows the result of the rotation matrix in the pictures. The scale of the movement is indicated as a colour scale from blue to red.

Secondly, the VO usually drifts especially on the pitch and roll directions (as described in [41]). Since the trajectories for this project were mainly across one floor, with flat terrain and predominantly two dimensional path, the z displacement and the pitch and roll variations were set to zero. The result is a much more accurate 3D map than the one that would be obtained if the 6DOF were being estimated.

It is very common to use a combination of Visual and Inertial sensing to get a more accurate estimation of pose. The purpose of using both is that they offer complementary char-

acteristics, with the Inertial system correcting the Euler Angles of the visual estimation. Many examples of such systems can be found in literature, such as in [41].

An Inertial Measurement Unit (IMU) was not available at the time of the experiments taken for this project, so such a combination could not be implemented. However, restricting the estimations to two dimensions led to similar results. Further advancements in the project would include having an IMU to make the estimation free in the 6DOF instead of restricting it to 3DOF.

In order to have a better insight on how the system perform in the real world, the histogram of percentage of inliers of the Visual Odometry measurements is plotted in Figure 8. This particular data was also collected from the "Edinburgh Dataset" referred in Section 6. This is using Multisense SL sensor running at 30Hz in real-time.

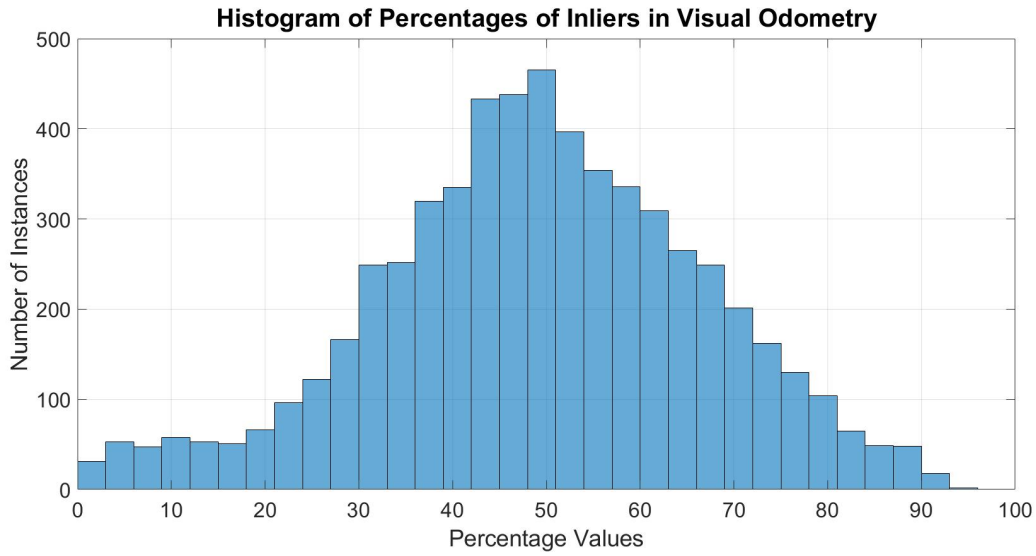

Figure 8: Histogram of percentage of inliers based on the Edinburgh Dataset

The dataset gathered approximately 6000 frames, and the mean of the number of features matched is 617. It can be seen that it is most likely to get at least 30% of inliers, which for practical purposes is enough to get a relatively good odometry estimate. However, the number of frames that have 0% to 30% inliers is significant. This contribute to the final drift and it is one of the reasons why the visual odometry system does not perform perfectly.

In order to get a better idea of how the feature matches changes with time, Figure 9 shows the distribution of feature matches and inliers by the frame number (which can be converted to time).

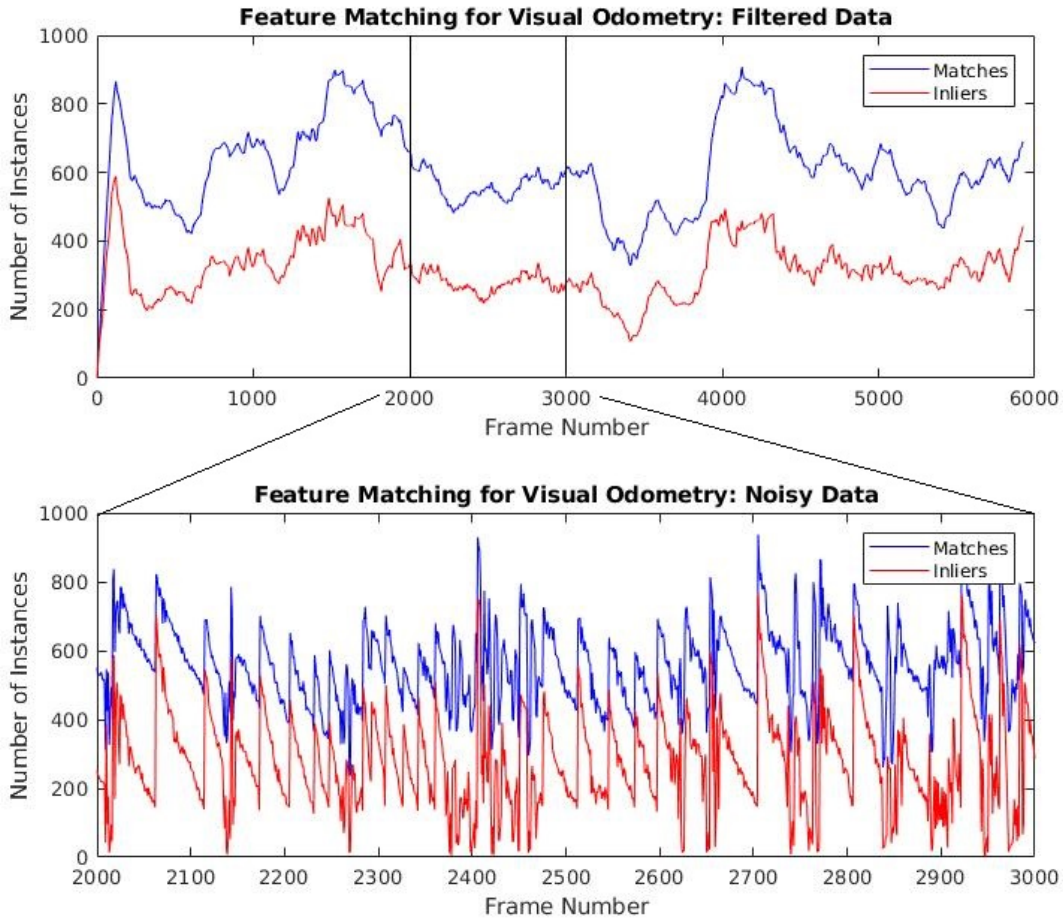

Figure 9: Matches and Inliers of the Visual Odometry system as a function of frame number. The top graph shows all of the frames, and it is a smoothed plot of the data, using a simple average filter with windows size equal to 120. The bottom graph shows the real (unfiltered) noisy data for the period between the 2000^{th} and the 3000^{th} frames.

As explained in Section 2.1, the quality of the visual odometry depends on the feature detection algorithm, which might fail or vary depending on the scene being filmed. In the top graph of Figure 9, the filtered data of the number of matches and the inliers in each of the frames can be seen, using a 120 point moving average filter. There is a clear trend in the data, where there is a smaller number of features being found in the period from frame 3000 and 4000. This indicates that at some places in the path, there are either less features being detected (for example, when the scene is showing a blank wall), or the mobile robot is rotating fast enough so that many features in one image is not found in the next.

The graph in the bottom shows a section of the noisy data corresponding to frames number 2000 to 3000. It can be seen that even when the graph is smooth and not varying in the

average number of matches and inliers (as shown in the top graph for the respective section), there is a high variance on the number of matches and inliers.

The peaks have periods of approximately 20 frames, and indicate when a new keyframe is selected. In order to reduce short-scale drift, FOVIS compares the features of each new image with a reference image, called a keyframe. Gradually over time, the sensor moves away from the current keyframe and therefore there are less matching features between the frames. When the number of matches reaches below a certain threshold, a new keyframe is selected. Whenever a new keyframe is selected, there is a higher number of features being matched, since many features can be seen in both images. This explains the triangular shaped periodic variation seen in the bottom graph.

Both of these long-term and short-term variations contribute to the overall drift of the system. This is corrected by the Laser Odometry as shown later in Section 4.2.

Wheel Odometry

Husky's platform includes a wheel encoder and an IMU, which together implement an EKF estimation of the robot's pose. Because this only uses proprioceptive sensors, this method causes the robot to drift over time. Overall, this method yields similar results to the Stereo Visual Odometry.

An interesting possibility that was not adopted in this project is to integrate both methods to try to produce a more precise estimation of the pose. Since the platforms used in this project had a LiDAR sensor available, this was used instead in order to get more accurate estimation results.

4.2 Laser Odometry

Given the first odometry measurements, it is clear that the resulting map does not look right **ADD IMAGE OR POTENTIALLY CHANGE WORDING (PIC OR DIDN'T HAPPEN)**. In order to improve the estimate of the trajectory, the next step is to use laser based localization using the Point Clouds from the trajectories.

As LiDAR are exteroceptive sensors, it is expected that laser based localisation achieves significantly less drift than using a proprioceptive sensor (like wheel odometry). However, since ICP algorithms are prone to failure depending on how inaccurate the first pose estimations are, there is a need to incorporate a robust method of incorporating laser based-localization.

For this reason, this project used the system described at [42] for laser odometry. This algorithm works in two phases: first it selects a point cloud as the reference of registration. Second, it calculates the prediction of failure of subsequent point clouds to register with the reference. If the prediction states that there is no failure, then the point cloud is registered to the reference, and it iterates to the next point cloud. If the prediction states that there is a sufficiently high risk of failure, then the point cloud becomes the new reference of registration, and subsequent point clouds are registered to this new reference frame.

The risk of failure is calculated using two parameters: the alignability and the overlap. First the overlap is calculated using the the range and occupancy from the first odometry measurements. After that, the alignability is calculated, which is a measure of how "constrained" in three dimensions the two point clouds are. This is to avoid the problem of registering two point clouds taken in a long corridor for example, where there will be many local minima since the path would be unconstrained in one dimension. From those two parameters, a model is learnt using Support Vector Classifier (SVC), and the Risk Prediction is drawn from that model. More details can be checked at [42].

Notice that the algorithm greatly reduces the short term drift. The main source of drift in this case is when the reference is changed. This leaves a small amount of drift at every changing of reference, which accumulates in the long run and yields a noticeable final drift.

The results for each of the paths are shown below for comparison. Figure 10 shows the results for the data collected with Husky using Wheel Odometry. It is noticeable the difference between the accuracy of the First Odometry Measurements to the Laser Odometry. However, it can be seen that there is drift due to how the AICP algorithm works.

Whilst this accumulated drift is unnoticeable from frame to frame, over a large enough distance the accumulated drift becomes significant. A way of correcting this long term drift is by using the loop closures.

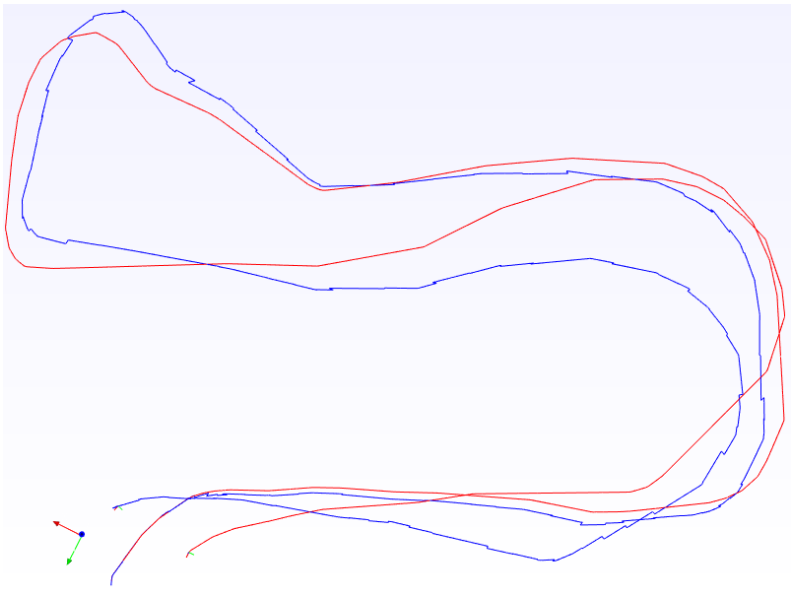

Figure 10: Result of the Wheel Odometry feeding the laser odometry system. The red path shows the Wheel Odometry and the blue path shows the corrected poses after being computed by the AICP algorithm. The discontinuities correspond to the locations where the ICP applied the transformation to correct the poses.

4.3 Loop Closure Detection

In order to adjust for the accumulated drift of the path estimate, a loop closure detection algorithm was implemented. Since it was assumed that the robot's drift would not be significantly large (it would not overdrift), three simple heuristics were used to detect loop closure: Time Sample Filtering, Euclidean Distance, and Pose Alignment.

- **Time Sample Filtering:** In order to avoid the problem of falsely identifying loop closures between two poses that are sufficiently close together such that the sensor never left the room, a time sample filtering was applied. The idea is to sample every S pose, so that the candidate loop closing poses would be sparse enough so that the loop just occurs between large time frames, but dense enough to apply Euclidean Distances.

- **Euclidean Distance:** Once the estimates have been sampled, the Euclidean Distance between each of them is calculated. If the distance between any two states is less than a threshold value E, then the two estimates form a candidate pair and they are added in the candidate pair list.

- **Pose Alignment:** After the Euclidean Distance Filter, the candidate pairs are tested for their relative pose. Because the loop closure correction relies on alignment of point clouds using ICP, it is a good strategy to select poses that would maximize the overlap between the point clouds associated with the candidates. In order to do that, another sampling is done based on the overlap between the field of view of the estimates. If the overlap is less

than a threshold value O, then the candidate pair is dropped out from the list, and the remaining are the loop closures that are considered.

The parameters S, E and O are chosen heuristically depending on what dataset is used in the algorithm. Changing the parameters can affect the outcome of the map significantly, so it is important to spend some time tuning them to the specific requirements of the test. Table 2 shows some results for the number of loop closures achieved when using different values for the parameters.

	$S=1$	$S=2$	$S=3$	$S=4$
$E=1$	62 | 6 | 4 | 3	15 | 0 | 0 | 0	7 | 2 | 0 | 0	5 | 0 | 0 | 0
$E=2$	188 | 35 | 22 | 13	42 | 6 | 4 | 1	21 | 2 | 0 | 0	9 | 1 | 0 | 0
$E=3$	447 | 90 | 61 | 35	77 | 10 | 6 | 2	33 | 4 | 1 | 0	18 | 1 | 1 | 0
$E=4$	735 | 152 | 108 | 57	120 | 15 | 11 | 2	50 | 6 | 3 | 1	30 | 2 | 2 | 0
$E=5$	1024 | 185 | 129 | 71	169 | 22 | 17 | 8	70 | 10 | 7 | 4	34 | 3 | 3 | 1

Table 2: Number of Loop Closures for different parameter values. The value of the parameters S and E are labelled in the columns and rows respectively. The values in each cell corresponds to the number of accepted loop closures when the value of O is equal to | No Filter | 45% | 50% | 55% | respectively.

It can be seen from Table 2 different values of the parameters give a significantly different number of loop closures. It is also can be shown that they vary in quality. For example, for the cell $S=1$, $E=5$, out of the 1024 loop closures found when no overlap filter is applied, only 185 (or 18%) have at least 45% overlap, which indicates that they are good loop closures. For the cell $S=1$, $E=1$, only 10% of the loop closures are good for at least 45% overlap. This illustrates how the quality of the map can be significantly changed based on the parameter values of this algorithm.

Figure 11 shows the results of the Loop Closure detection when applied to the "Edinburgh Dataset". Due to the relatively low velocity of the mobile robot, the parameters were adjusted to match the time that the mobile robot would take to leave a room before coming back to the same room.

It is also important to notice that marginally different parameters have an impact on the number of loop closures and on the outcome of the map. Figure 12 shows the results of different maps according to different settings of the loop closure parameters.

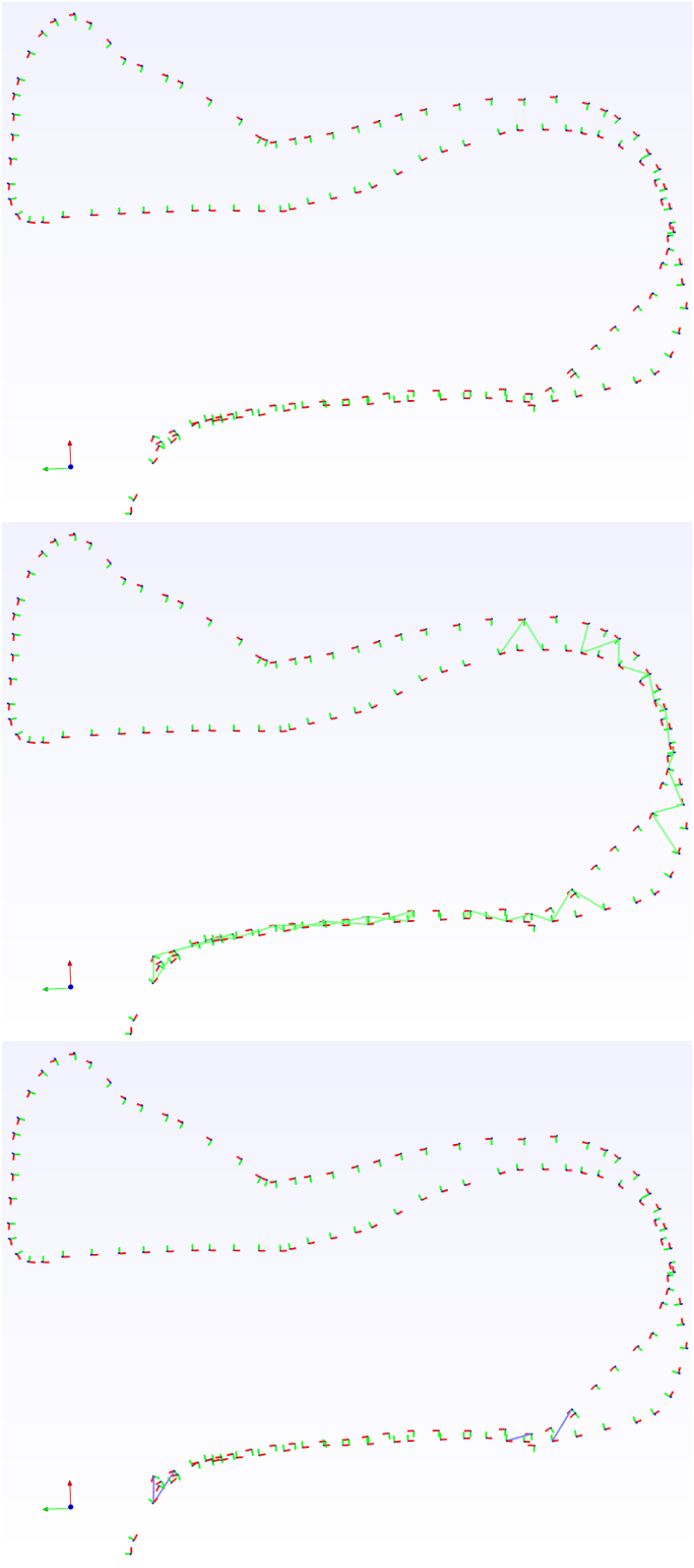

Figure 11: The three heuristics for loop closure detection. Data shown was collected using the Husky Mobile Robot and the Velodyne LiDAR, visualized in bird's-eye view with red and green coordinates representing the path of the robot. The figure on the top shows the result of the time sampling. The plot in the middle shows the Euclidean Distance Pairings. The last figure is the result of the Pose (overlap) filter. In this experiment, $S = 2$, $E = 2$ and $O = 0.5$.

The assumption that the drift in two loop closures is relatively small is not always valid. For cases when the drift is sufficiently big, other methods for finding loop closures have to be implemented. A popular approach is to find loop closures from images, where each frame is compared given some descriptors and if two scenes look similar enough, they are considered as a loop closure. This is a more sophisticated and accurate system. However, since this project is concerned with indoors mapping, it is assumed that a substantial amount of loop closures will be available in a relatively short time frame. This validates the loop closure system used. Further work in this area would be necessary to make the system more robust to large drifts.

Ideally, the number of loop closures should be neither too big nor too small. Loop closure can be thought of strings "tightening" the Factor Graph in Figure 3 by adding constraints to it. If many loop closures are made, the graph becomes too constrained and new corrections to

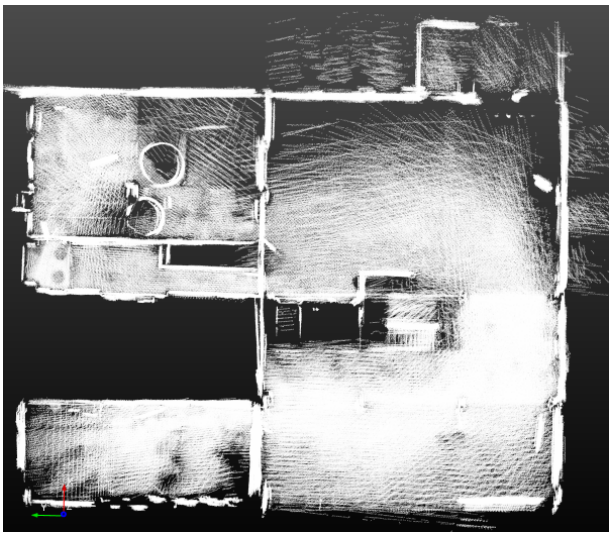

(a) $S = 1; E = 2$

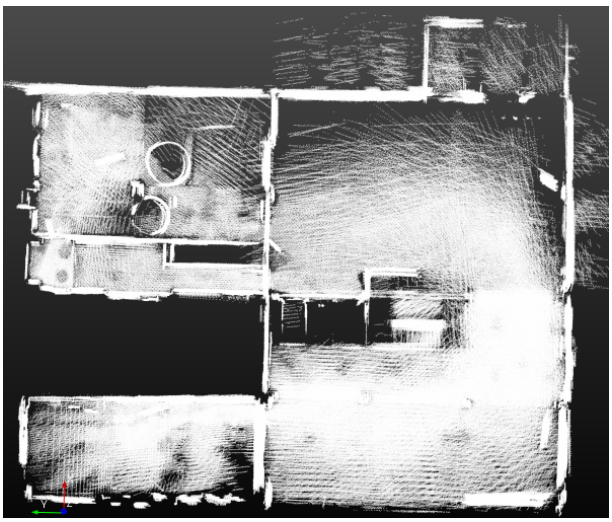

(b) $S = 2; E = 3$

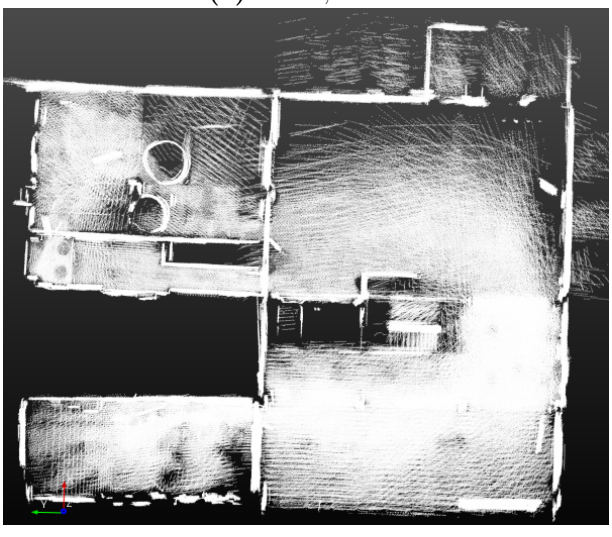

(c) $S = 1; E = 4$

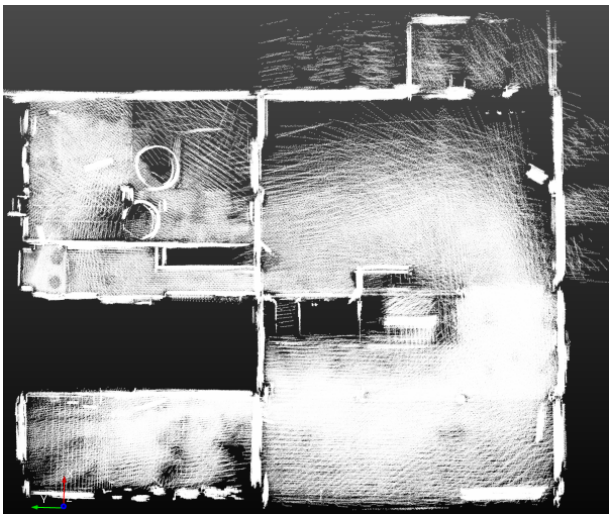

(d) $S = 3; E = 5$

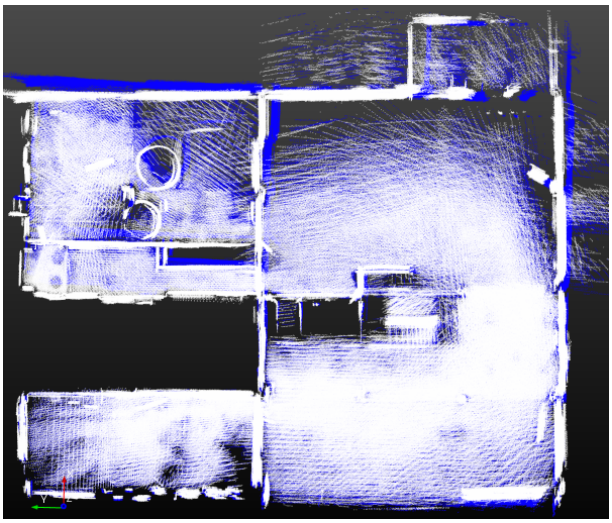

(e) (c) and (d) superimposed. (c) in white and (d) in blue

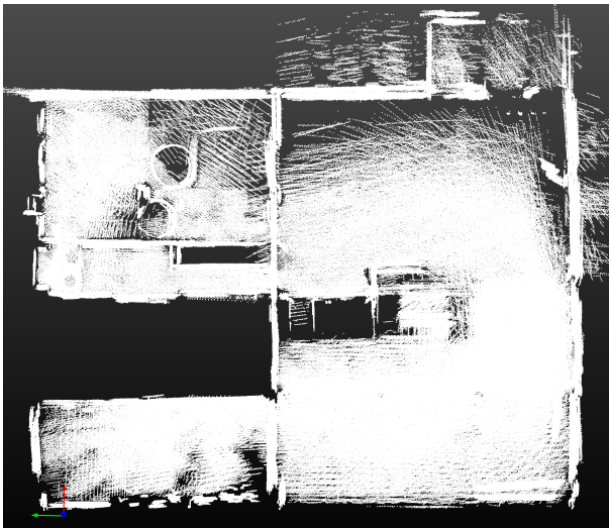

(f) No Loop Closure

Figure 12: Results of applying different values of the S, E and O parameters for the same dataset. All of the images use $O = 45\%$ It can be seen that they give noticeably different maps, even though they are all better than the no loop closure map. This is shown by looking at the top right corner and the bottom right corner of the images, which shows that in the no loop closure is the one that the walls are noticeably not superimposed.

the map would be insignificant. This can be naively desirable since it means that the certainty of the graph is high, but if one loop closure has some error, then the effect cannot be corrected subsequently. On the other hand, if few loop closures are made, then the drift between poses are not corrected substantially and the overall error in the graph is high.

Therefore it is crucial to tune the parameters so that meaningful loop closures are selected.

Front End Loop Closing Problem. One of the biggest problems with loop closing is that it has a massive effect on the topology of the map. If for some reason either the loop closure is not a good one or if the point cloud registration is inaccurate, the effect on the map is disastrous (just as demonstrated in [43]).

Unfortunately, ICP algorithms are known for having multiple minima points, which means that not always the registration converges to the global minimum point. Even worse, sometimes the global minimum point might not even be the right registration, maybe due to ambiguities in the map (consider the long-corridor problem and registering a point cloud in the long-corridor).

This brought up the problem of multimodaility: because the ICP is not a convex function, there are multiple minima to which the algorithm could converge. If the wrong registration point is the one detected by the algorithm, then it would introduce an almost irreversible error in the map, and make it more difficult to reconstruct it accurately in the 3D reconstruction system.

Many systems and algorithms could be used to avoid this problem, including multihypothesis and a stronger front end selection key. In the project, it was chosen to select the loop closure by hand (i.e. by adjusting the parameters such that appropriate closures are detected) due to the lack of time to implement a multihypothesis system. That is however an area that should be explored in future projects.

4.4 Graph Optimization

As presented in Section 2.2, many graph optimization tools were created. In this project, the Graph Optimization was conducted using the iSAM library. Since the exteroceptive model used was LiDAR data instead of any landmark localizer (like Visual Data or Fiducial Systems for example), a pose-only graph is generated.

A pose constraint-based SLAM follows from the landmark based SLAM. The difference is that instead of using landmarks as a way of localization and mapping, the odometry measurements are used to connect subsequent pose estimates and the loop closures connect two arbitrarily distant poses. This is a common method of SLAM systems when using dense laser range-finder data, such as the LiDAR sensor used in this project.

Just like with its landmark counterpart, the pose only system can also as easily be modelled using graph models introduced in Section 2.2. We can model the dependencies of the variables using Bayes Networks as well.

Framing the model above mathematically, the total probability is given by:

$$P(X,U,C) \;\propto\; P(x_0)\prod_{j=1}^{M} P(x_j|x_{j-c},c_j)\prod_{i=1}^{M} P(x_i|x_{i-1},u_i) \tag{3}$$

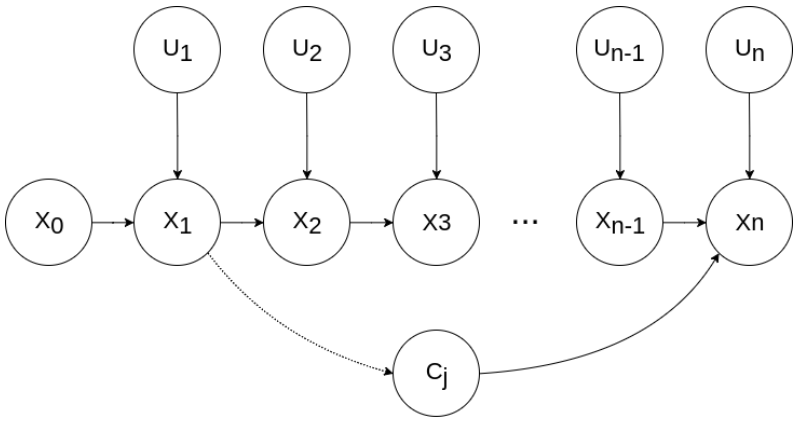

Figure 13: Pose only SLAM as a Bayes Net. The dotted line from x_1 to c represents the parameter used for the loop closure. The value $\mathbf{x_0}$ denotes a prior; $\mathbf{x_n}$ denotes the state vector; $\mathbf{u_n}$ denotes odometry measurements; $\mathbf{c}$ denotes close loops.

The loop closures C_j act just like odometry measurements. They are computed using the ICP algorithm as described in Section 4.3. They are treated separately in the iSAM algorithm, which includes another constraint to the system. As described in [20], loop closures add many non-zero entries in the factor matrix. This results in added complexity and increase in computational burden. However, they are very important for long-term drift free localization and mapping, as discussed in Section 2.2. It is important to notice that all of the SLAM properties for landmarked based systems also hold for Pose-Only based systems [20].

The results of the Wheel Odometry system when applied the Optimization are shown in Figure 14. Both figures show the point clouds collected in the experiment, which can be used to understand how well the localization algorithm performs. In the figure on the left, the different colours represent different timestamps in which the point cloud was taken, starting with blue, going cyan, then yellow, orange, before finishing with red.

It can be clearly seen that the figure on the left does not show any apparent drift in the short term. Each of the individual close point clouds seem to be aligned. This can be noticed by looking at point clouds of the same colour. For example, the point clouds with orange colour seem to be perfectly aligned with each other. This indicates that short term drift is small.

However, when comparing point clouds that have different colours (for example, the blue and the red), it is clear that in the long term, the robot has drifted significantly. This long term drift is only apparent when the robot goes back to the same room, which can be detected using the algorithm as described in Section 4.3.

The figure on the right shows the map after the point clouds have been aligned. Comparing the bottom right corner of the two figures (the red and blue point clouds) and the top

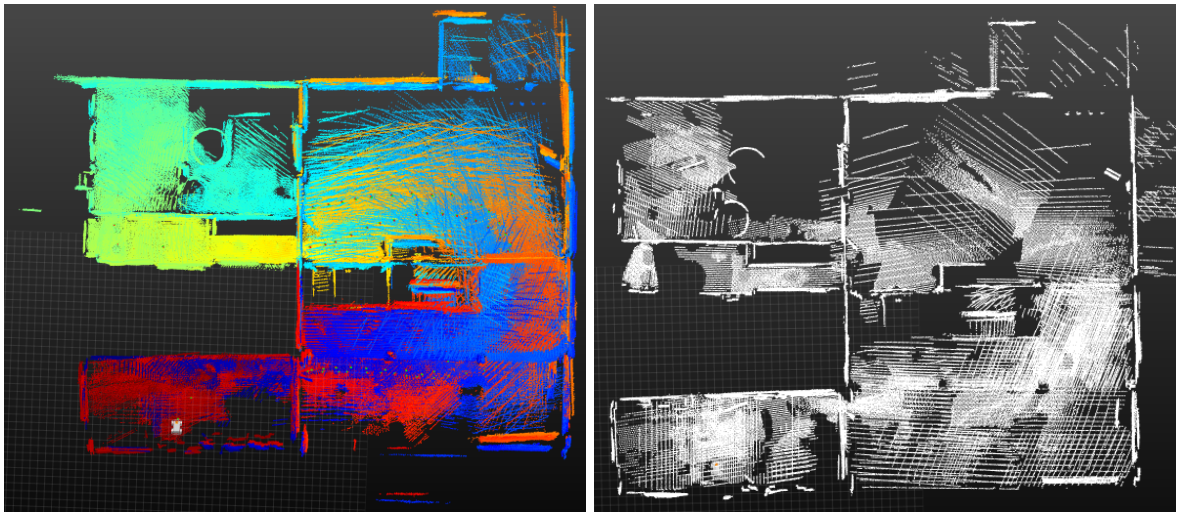

Figure 14: Result of the Graph Optimization solution. The map in the left shows the Point Clouds collected without Graph Optimization and Loop Closures applied. The map in the right shows the result of the map after the loop closures have been implemented in the iSAM algorithm. Notice the alignment of the wall at the top of both images and at the very bottom to compare the overall drift of both systems. The point clouds in the picture in the left are coloured with timestamps.

right corner (the cyan and orange point clouds), it can be seen that the figure in the right manages to align the long term drifts satisfactorily.

This is an important result, since global alignment of the point clouds is crucial for the 3D reconstruction described in the next section. In this way, we avoid doubled walls and open the opportunity for more flexibility when defining the hyperparameters of the 3D Reconstruction System.

5 Integration with BOR²G-CUBES

As explained in Section 3, the result of the Graph Optimization is then input to BORG-CUBES. Since this algorithm was built to reconstruct cities with an eye at autonomous driving, it requires a sufficiently dense representation of the LiDAR point clouds. Unfortunately, this is not the case for mobile robots operating indoors with a single LiDAR sensor.

Furthermore, BORG CUBES adopts a framework that can regularize the reconstruction based on the Total Variation. Putting it simply, the idea is to optimize a cost function that penalizes high derivatives. It is of the form below:

$$\min_{u} \int_{\Omega} |\nabla u| d\Omega + \frac{\lambda}{2} \int_{\Omega} ||u_i - f_i||^2 d\Omega \tag{4}$$

In Equation 4, the first term shows the total variation cost. This is the term that emphasizes that the data must be processed in order make it smoother. The second term is the data fidelity cost, which is responsible for making the structure resemble the observations of the data.

The hyperparameter λ is set by the user and it dictates how much weight each of the two terms are going to have. Different than a normal regularization framework, this term sets how much fidelity to the data the regularized model is going to have. A high value for λ indicates that the model should be closer to the unregularized model even though it might mean being noisy. A low value for λ means that the regularized model should be smoother, even though it means being less similar to the data.

Figure 15 shows some results of changing the lambda parameter for some models. Even though regularizing the map yield a smoother reconstructed surface, it also excludes surfaces that are in general disconnected from other surfaces, as can be seen in the next figures.

There are also a couple of hyperparameters that needs to be set when using any 3D reconstruction system. The most important one is the edge length. This sets the size of each voxel in the voxel grid. The bigger this number is, the more "pixelated" the reconstruction is going to be. The smaller this number is, the more detailed the map is going to become.

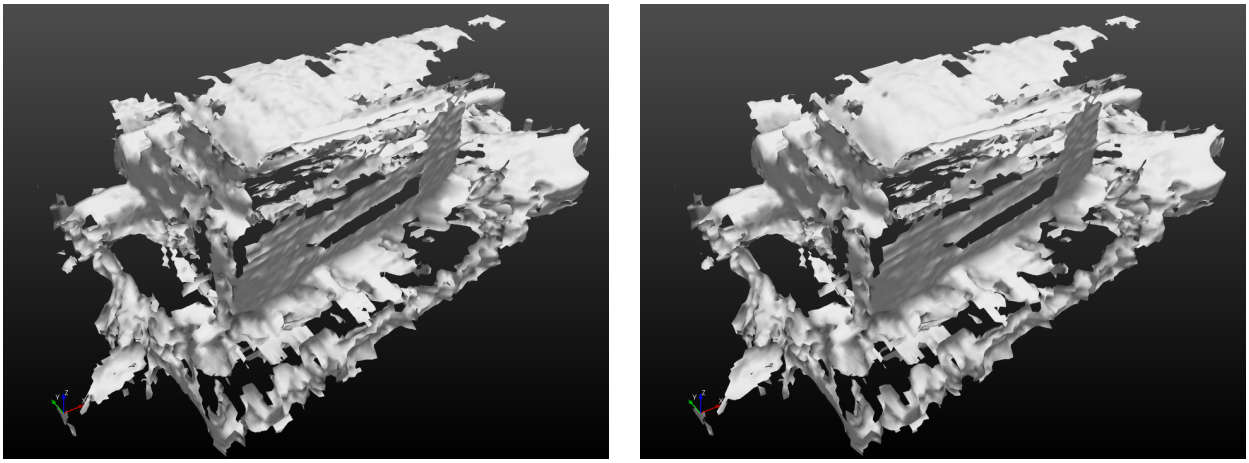

(a) $\lambda \to \infty$ **(b)** $\lambda = 1$

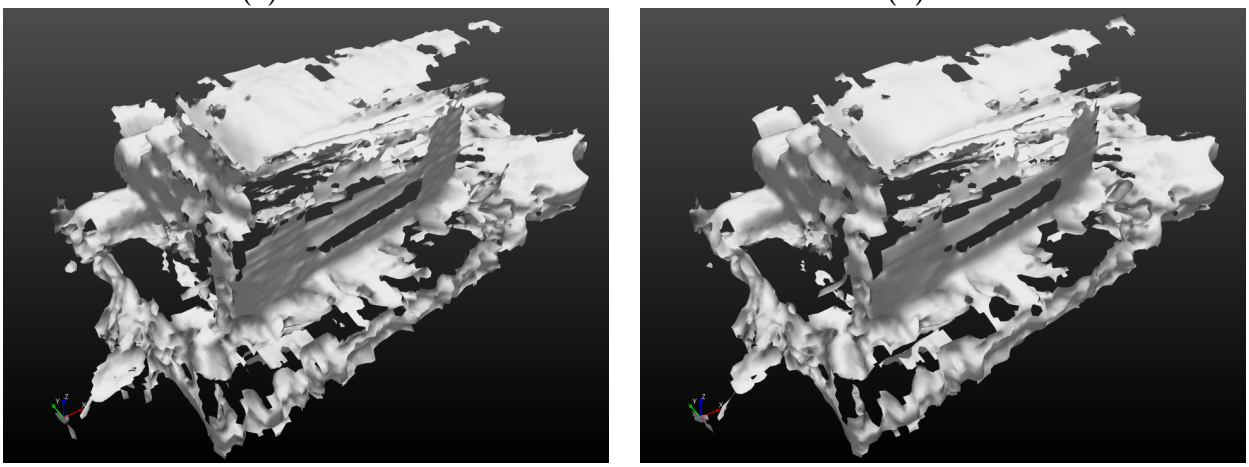

(c) $\lambda = 0.5$ **(d)** $\lambda = 0.1$

Figure 15: Model with different λ values for the regularizer. It can be seen that the surfaces get smoother the smaller the value of λ is.

There is an important trade-off when determining this value. For object-centered small-sized reconstructions, such as KinectFusion [4], a small side-length of the voxels would mean greater resolution of the reconstructed scene. KinectFusion for example sets this value to 1.95mm, so that a 256^3 voxel block would mean a $0.5^3 m^3$ volume. For large scales though, that would mean too much memory having to be allocated. BORG CUBES for example sets the size length to 0.2m.

Figure 16 shows the result of different edge lengths applied to a model. It can be seen that the lower the value of the voxel edge, the more detailed the model becomes. However, this results in sparser surfaces, since small voxel sizes mean that many of them are empty, which results in unconnected surfaces. A very large voxel size might result in surfaces being blended such that the overall shape of the building is not properly captured.

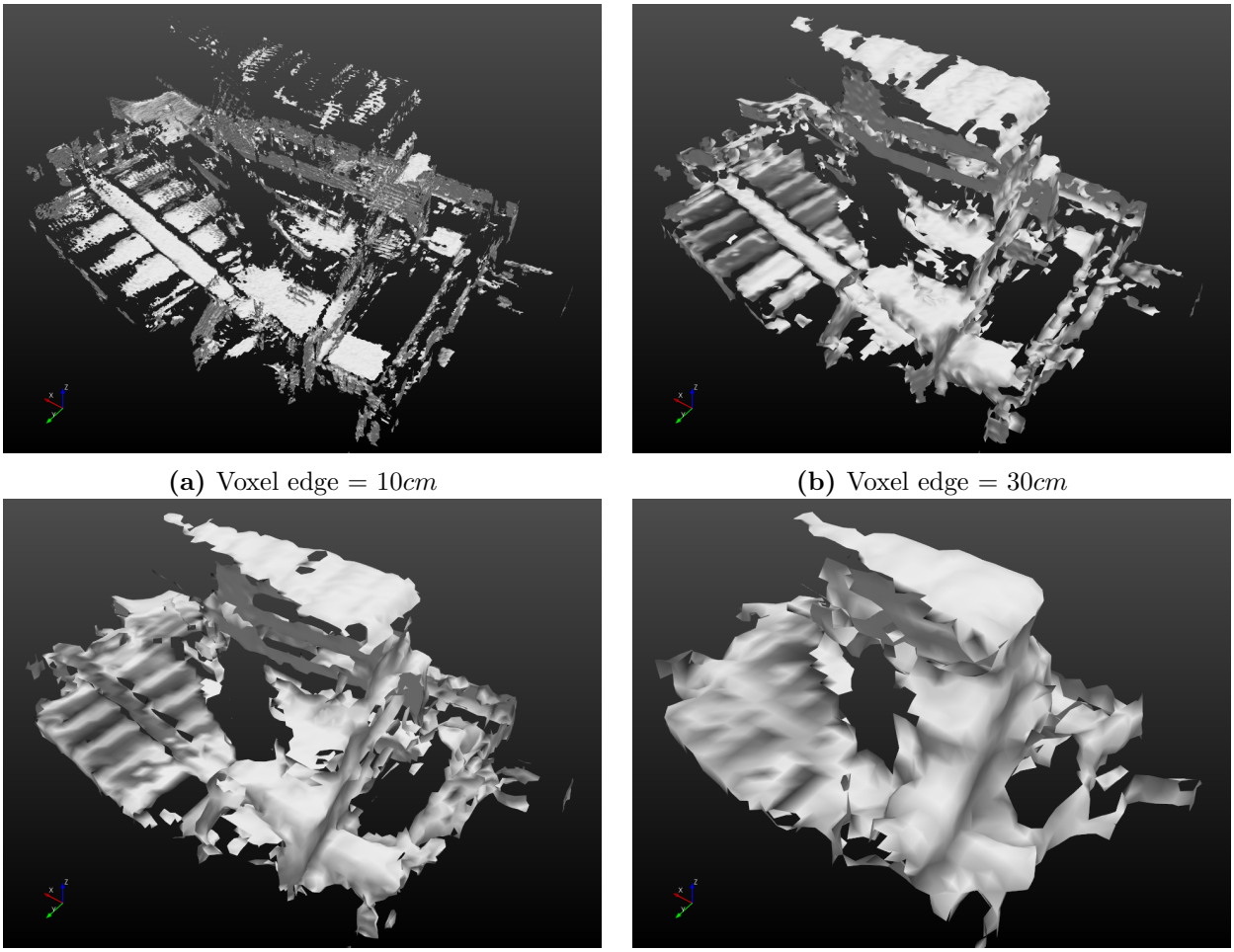

(a) Voxel edge = $10cm$ **(b)** Voxel edge = $30cm$

(c) Voxel edge = $50cm$ **(d)** Voxel edge = $1m$

Figure 16: Models with different Voxel Edge Length values for the fusion.

Ideally, we would expect that smaller voxel edges would make the reconstruction look more realistic. As demonstrated in KinectFusion [4], very small voxels yield models that closely resemble reality. When reconstructing big environments though, a bigger importance is placed on the overall shape of the building rather on the small details. One could say that for planning in big environments, low frequencies should outweigh high frequencies.

Also as expected, the determination of all of these aforementioned hyperparameters is more of an art than a science. Different parameters might work better in different environments and applications, using sensors with different accuracies. In general, large-scale reconstructions require larger voxel edge lengths to account for limited memory, and the λ regularization term varies between 0.5 to infinity (which is basically no regularization), which can account for limited computation power.

6 Experimental Results

This pipeline was tested in two different datasets: the Edinburgh dataset and the Information Engineering Building (IEB) dataset. In both of them, the sensors did not contribute to planning nor control of the motion, but rather they were moved independently for the data collection.

The sensor used to collect these datasets was the MultiSense SL [10], which is a tri-modal sensor: it provides laser data, - from a Hokuyo UTM-30LX-EW [11]- 3D stereo data, and RGB video. The laser spin was set to 15RPM for both of the datasets. The aperture time for the stereo camera can be changed, and in both of them it was set so that it would compensate the light condition of the experiments.

6.1 Edinburgh Dataset

This dataset is the same used in [42] (though referred as the IF dataset in the paper). This is an approximately 180 meters path. It passes through 5 doorways in 5 different rooms of varying sizes. It collects data in an area of approximately 27m x 32m, with a maximum height of approximately 20 meters, which is achieved in the two big rooms. It contains static objects (such as tables and chairs) and moving people. It is a one big loop path, which is convenient for the loop closure detection.

There were 117 scans in total, each having approximately 60000 points. A top view of the map is shown in Figure 17. The numbers are labelling the different rooms of the environment. In the experiment, the robot travelled from rooms 1 to 5, and returned to 3, then 2 and finally 1. As it was explained in Section 4.3, the parameters to select the loop closures play an important role when compiling the final map. In this case, the parameters were set so that 5 loop closures were identified: one in room 3, two in room 2 and two in room 1. When compared to the map shown at [42], it is clear that there is no accumulated drift due to odometry measurements in room 1. The map created then is accurate enough to be used as an input to the reconstruction algorithm.

The results of the final reconstruction of this system is shown in Figure 18. The

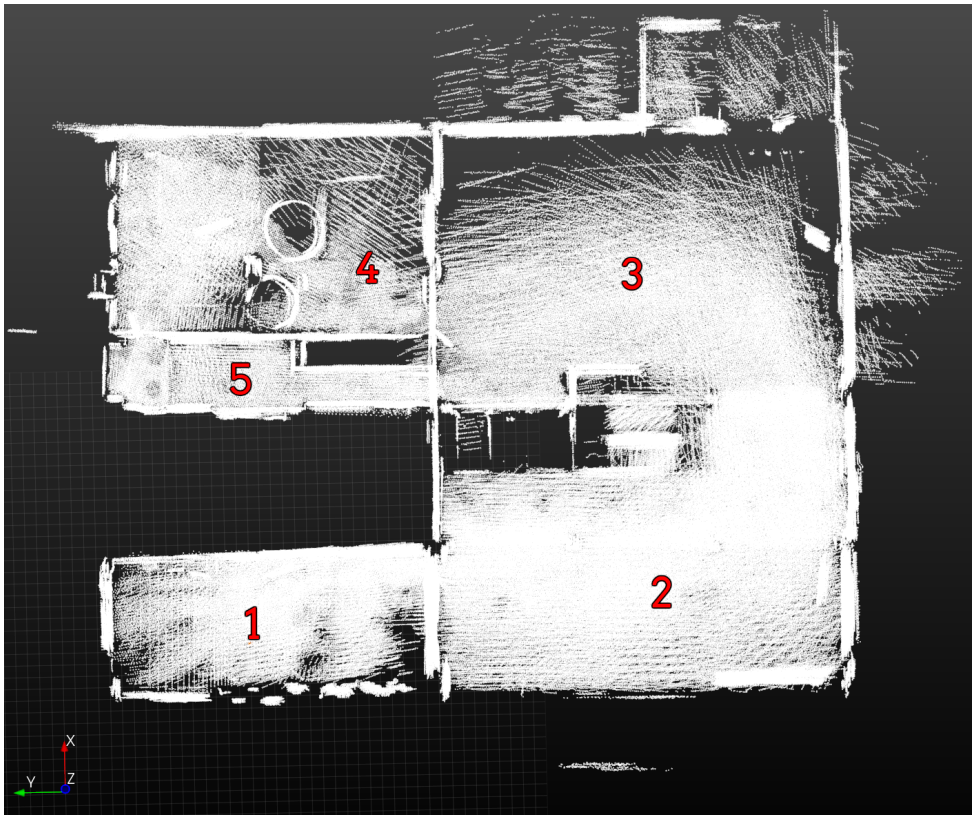

Figure 17: Bird's Eye view of the map of the Edinburgh Dataset. The path taken was 1, 2, 3, 4, 5, 3, 2, 1. Loop Closures were detected in rooms 3, 2 and 1.

first row of the figure contains the raw point clouds collected and arranged after the SLAM algorithm outputs the trajectory of the robot (with loop closure included). It can be seen that even though the point clouds are dense in some walls and in some of the roofs, there are some areas of sparseness. In particular, corners, windows and some of the walls have a low number of points if any at all! This is expected, since the laser data only collects points if the laser is reflected back to the sensor, which might leave holes depending on the surface that it is trying to reconstruct.

The second row and third rows show the point clouds after being inputted to the 3D reconstruction system. The results naturally depend on some hyperparameters, as explained in Section 5. This figure shows results for edge-length equals to 0.2m. It can be seen that the surfaces are generally rough and noisy, due to imperfections in the laser scan data and in the inaccuracies associated with the SLAM solution.

The fourth and fifth rows show the results of regularizing the system using a λ factor of 0.1 and number of iterations equal to 50. It is clear that by performing this regularization,

Edinburgh Dataset

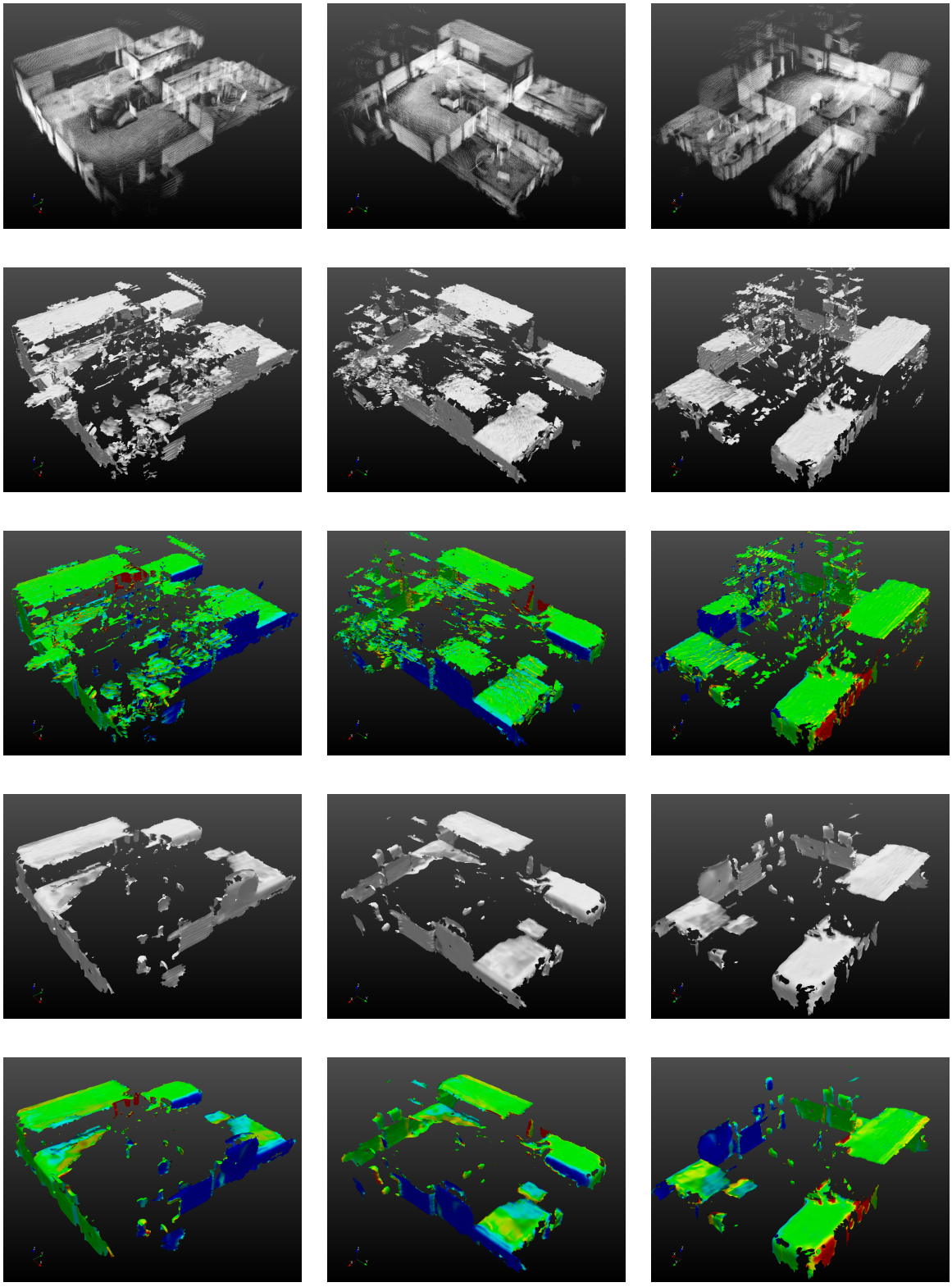

Figure 18: Results of running BORG CUBES to point clouds from first row. Second and third rows shows unregularized reconstruction (solid and normals coloured). Fourth and fifth rows show regularized reconstructions with $\lambda = 0.1$ and 50 iterations (solid and normals coloured).

many unconnected surfaces were removed, which was interpreted as noisy measurements due to the high variational components. The surfaces that remained are mostly long connected walls and roofs, which are significantly smoother than the unregularized reconstruction. It can also be seen that some of the corners were smoothed, which actually should be sharp corners. This is expected since the TV regularizer penalizes high variational profile, which ends up smoothing corners.

6.2 Oxford's Information Engineering Building Dataset

This dataset was collected specifically for this project. A trolley was used to mount the MultiSense SL as shown in Figure 19. The trolley then was pushed at walking speed through the first floor of the Information Engineering Building at Oxford. A video of the data collection process is available at [44]. The sensor goes through 2 loops, travelling approximately 210 meters. It passes through 10 doors, one big room with a maximum height of approximately 15 meters. It also contains static objects and moving people.

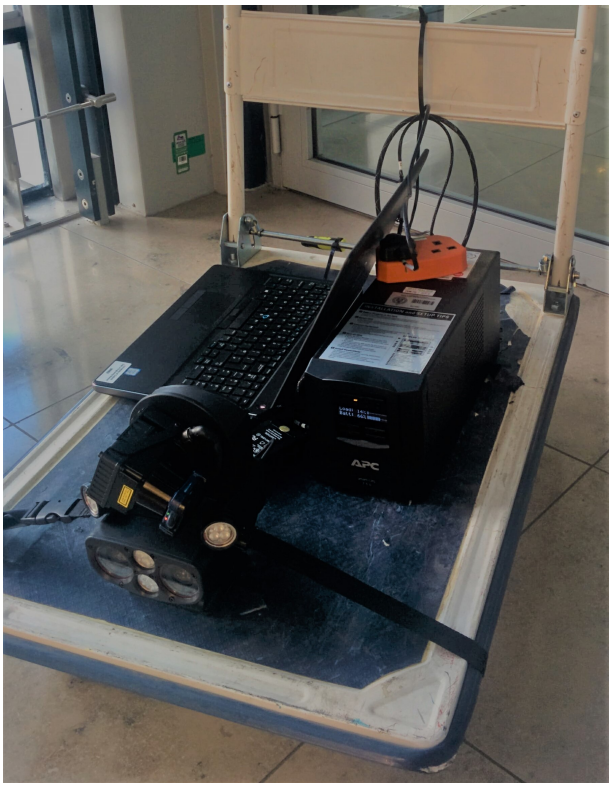

Figure 19: Sensor support apparatus. It includes the MultiSense SL in front with an UPS (Uninterrupted Power Supply), and the laptop for logging data.

Since this dataset is more segmented than the Edinburgh dataset and the loops are performed in two different sections, it was more sensitive to the parameters set by the loop closure system. It is also noted that there are significantly more windows in the Information Engineering Building (IEB), and combined with the faster velocity of the sensor have made the point clouds less dense.

In total, 160 point clouds were collected, with approximately 60000 points per point cloud. The full path of the sensor and the position of the loop closures can be seen in Figure 20.

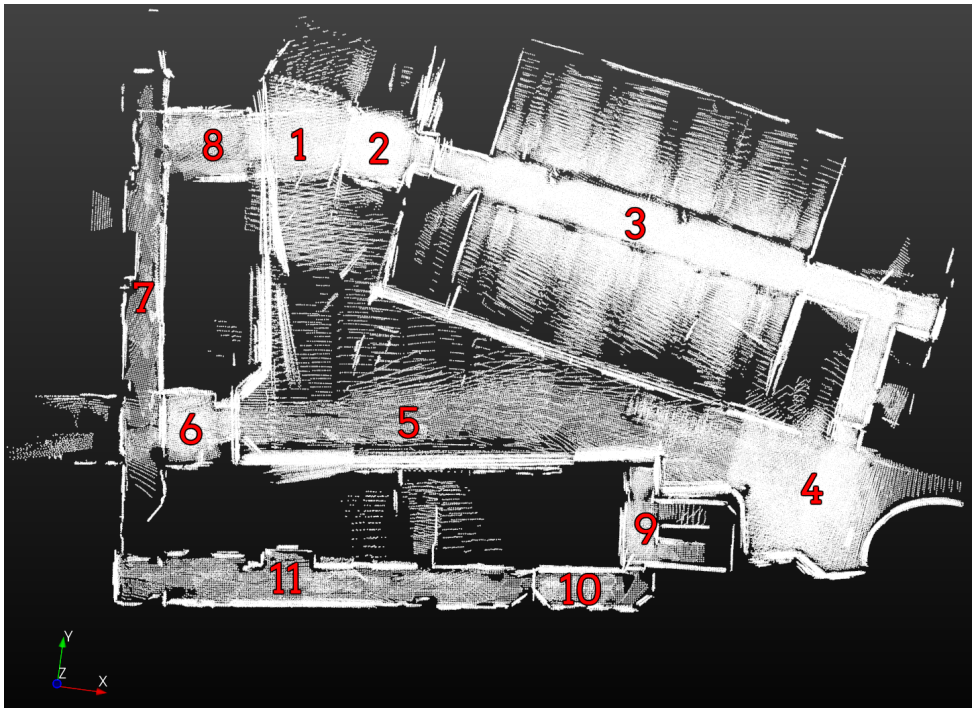

Figure 20: Bird's Eye view of the map of the IEB Dataset. The path taken was 1, 2, 3, 4, 5, 6, 7, 8, 1, 2, 3, 4, 9, 10, 11, 7, 8, 1. Loop Closures were detected in rooms 1, 2, 3, 4, 7, 8.

In the figure, the numbers are labelling the different rooms that were explored during the experiment. The path taken was from 1-8, then 1-4, 9-11, then, 7, 8 and finally 1. Therefore, two big loops were made, which was convenient to test multiple loops in the environment. Loop closures were detected in the rooms expected (1-4, 7 and 8). This was a more challenging problem to tackle than the Edinburgh dataset. The reason for this is that the loops were made in longer distances, which means that the drift accumulated between them were higher, and thus it made it difficult to identify loops using the heuristics outlined in Section 4.3. However, even in longer distances the system performed well and a relatively accurate map of the building could be generated. This map was then input to the 3D reconstruction system.

The results of the 3D reconstructed model after the SLAM solution can be seen in Figure 21. The first row shows the raw point clouds. For this dataset, the assumption about sparsity in corners and in windows is also valid. It can be seen that the corners are sparser than walls and roofs.

The second and third rows show the reconstruction without any regularization. Since the point clouds were sparser here, different parameters were used. The voxel edge length was set to 0.3m and the fusion threshold was set to 8. Noticeably, the corridor in the first picture

Oxford's Information Engineering Dataset

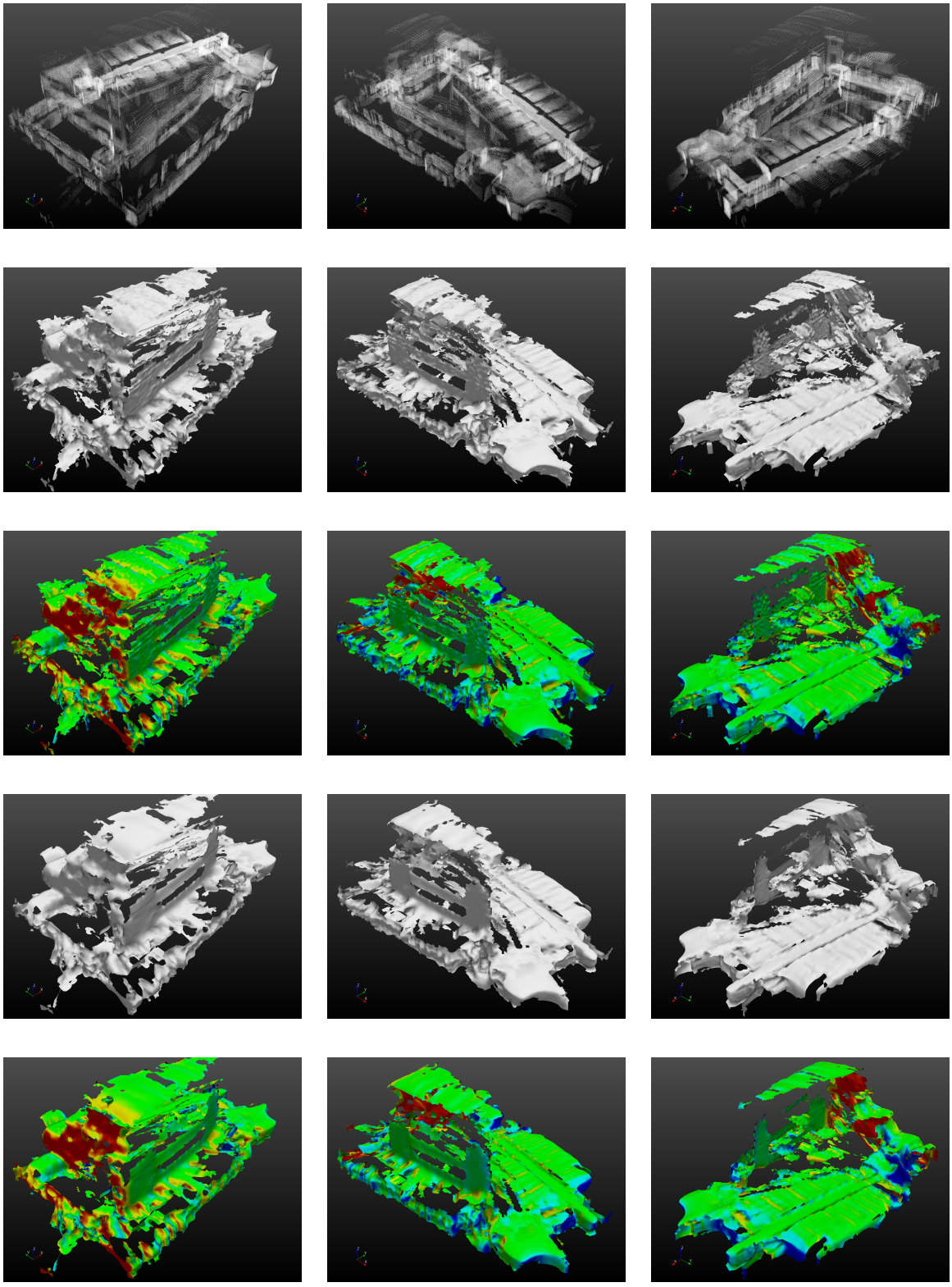

Figure 21: Results of running BORG CUBES to point clouds from first row. Second and third rows shows unregularized reconstruction (solid and normals coloured). Fourth and fifth rows show regularized reconstructions with $\lambda = 0.1$ and 50 iterations (solid and normals coloured).

from left to right of the second row got its walls merged. That is because this corridor is narrow, and the increase in the voxel edge length and the fusion threshold cause points in different walls to be merged together. A decrease in either of those two parameters would mean less surfaces being reconstructed though. So there is a trade-off when narrow spaces are concerned.

The fourth and fifth rows show the reconstruction using a λ of 0.1 and 50 iterations. It is noticed that the surfaces got smoother than the original reconstruction, and again some surfaces were removed as they were interpreted as noise by the algorithm.

6.3 Final Evaluation

In general, the two maps above have many holes in the final reconstruction. Those are due to the lack of LiDAR points in certain areas. When applying this pipeline to real-life applications, many strategies can be taken to overcome this problem. To cite a few: (i) Many LiDAR sensors could be used instead of just one; (ii) The robot could move slower to map the entire building and get denser representations of the environment; (iii) Other sensors could be embedded, such as visual and depth sensors.

As explained in the last Section, the parameters for the reconstruction can be arbitrarily set based on limitations on the hardware or specific applications for the whole pipeline. The ones chosen at the experiments were set with the intention of providing the best visual representation of the performance of the algorithm.

7 Conclusion

In this project, it was shown a setup that solves the SLAM problem and reconstructs a large-scale indoor environment using only LiDAR data. The system can be implemented in real time and incrementally, since all of the algorithms used are incremental solutions.

In such a broad and big problem, there are a couple of issues in the system that needs to be addressed in subsequent projects:

Loop Closure: The loop closure system as implemented is simple enough for small drifts in a structured environment. However, it is very sensitive to changes in the parameters. As it was shown in Section 4.3, different parameters yield significantly different maps, which is not good for a robust and embedded solution. Also, this solution does not take into account larger drifts. If a mobile robot does not perform loop closures in a relatively small amount of time, it might drift so much that the heuristics used (especially the Euclidean Distance) would remove this possible closure immediately. Other solutions taking into account visual cues (as extensively described in the literature) would have to be implemented to take those into account.

Multihypothesis: Related to the Loop Closure problem, it is needed a robust solution to prevent wrong loop closures from happening. Regardless of how the loop closure system is implemented, it will make mistakes, and those can be catastrophic to the final map. A robust solution then is necessary to avoid that small perturbations in the loop closing problem lead to totally erroneous maps being created.

3D Reconstruction: In this report, RGB or depth images were not used in the 3D reconstruction. As explained in Section 5, this is because RGB data are less effective for long distances and depth images are not suitable for outdoors applications. However, without RGB data, a sparse map is generated, since only LiDAR data is available for the 3D reconstruction. Since BORG uses sensor-agnostic voxels, it would be convenient to try a denser data generation, which would result in better maps.

Outdoors Experiments: It would also be beneficial to test this system in a dataset that is mainly outdoors. All of the sensors used are suited for outdoors applications, so the system should perform as expected. However, real life validation would have to be taken to agree with the theoretical grounds.

In general, the results show an exciting possibility of future systems having the ability to perceive indoors (and outdoors) environments in real time using only LiDAR data. By applying the changes suggested in this conclusion, and possibly including more LiDAR sensors, it is expected that the map will be reliable enough to use the result for path planning for example.

It is also interesting to compare this type of system with how humans perceive information. This report shows how the map generation problem is closer to achieve human performance. A big difference on how humans work and how systems of the type described in this paper work though is that humans also have prior information. Humans' brains that can fill in the information that the stereo visual system could not have gathered, and therefore are able to have a richer idea of what the environment looks. For example, for the plots in Figure 21, a human would easily be able to fill in the holes since they know that indoors environment usually have right corners and sharp edges (what Caughlan and Yuille called the "Manhattan world assumption" [45]). Incorporating such assumptions in the system is not an easy task however, since those "off-the-shelves" assumptions are not always right and they can distort the map so that details are not seen (see [46] for an example system that uses the "Manhattan World Assumption" for reconstruction using point clouds).

Also, humans can perceive semantic information (i.e. recognize what is a kitchen and what is a bedroom), which is much more complex than conveying geometric information. This also helps in the "filling the hole" problem, for example by knowing a priori what a tree looks like, humans would easily be able to fill the holes of the part of the tree that were not seen before.

In conclusion, the results that can be obtained at this point using only LiDAR are impressive. However, there is much work to be done to get to human-level performance. This is a promising time for the evolution of perception systems, and it is expected that new methods to leverage results will be arising in an increasing pace.

References

[1] H. Durrant-Whyte and T. Bailey, "Simultaneous localization and mapping: part i," *IEEE Robotics Automation Magazine*, vol. 13, pp. 99–110, June 2006.

[2] M. F. Fallon, M. Antone, N. Roy, and S. Teller, "Drift-free humanoid state estimation fusing kinematic, inertial and lidar sensing," in *2014 IEEE-RAS International Conference on Humanoid Robots*, pp. 112–119, Nov 2014.

[3] E. B. Goldstein and J. Brockmole, *Sensation and perception.* Cengage Learning, 2016.

[4] R. A. Newcombe, S. Izadi, O. Hilliges, D. Molyneaux, D. Kim, A. J. Davison, P. Kohi, J. Shotton, S. Hodges, and A. Fitzgibbon, "Kinectfusion: Real-time dense surface mapping and tracking," in *Mixed and augmented reality (ISMAR), 2011 10th IEEE international symposium on*, pp. 127–136, IEEE, 2011.

[5] H. Sarbolandi, D. Lefloch, and A. Kolb, "Kinect range sensing: Structured-light versus time-of-flight kinect," *Computer vision and image understanding*, vol. 139, pp. 1–20, 2015.

[6] R. Horaud, M. Hansard, G. Evangelidis, and C. Ménier, "An overview of depth cameras and range scanners based on time-of-flight technologies," *Machine Vision and Applications*, vol. 27, no. 7, pp. 1005–1020, 2016.

[7] O. Wasenmüller and D. Stricker, "Comparison of kinect v1 and v2 depth images in terms of accuracy and precision," in *Asian Conference on Computer Vision*, pp. 34–45, Springer, 2016.

[8] F. Pece, J. Kautz, and T. Weyrich, "Three depth-camera technologies compared," in *First BEAMING Workshop, Barcelona*, vol. 2011, p. 9, 2011.

[9] "Bumblebee datasheet." `https://www.upc.edu/sct/en/documents_equipament/d_186_id-488.pdf`. Accessed: 2018-04-28.

[10] Carnegie Robotics, "Multisense sl," 2018.

[11] "Hokuyo utm-30lx-ew datasheet." `https://www.hokuyo-aut.jp/search/single.php?serial=170`. Accessed: 2018-04-28.

[12] "Multisense sl description." `https://carnegierobotics.com/multisense-sl/`. Accessed: 2018-04-28.

[13] C. Cadena, L. Carlone, H. Carrillo, Y. Latif, D. Scaramuzza, J. Neira, I. Reid, and J. Leonard, "Past,present, and future of simultaneous localization and mapping: Towards the robust-perception age," *IEEE Transactions on Robotics*, vol. 32, no. 6, pp. 1309–1332, 2016.

[14] M. Montemerlo, S. Thrun, D. Koller, and B. Wegbreit, "Fastslam: A factored solution to the simultaneous localization and mapping problem," in *In Proceedings of the AAAI National Conference on Artificial Intelligence*, pp. 593–598, AAAI, 2002.

[15] F. Dellaert, D. Fox, W. Burgard, and S. Thrun, "Monte carlo localization for mobile robots," in *Proceedings 1999 IEEE International Conference on Robotics and Automation (Cat. No.99CH36288C)*, vol. 2, pp. 1322–1328 vol.2, 1999.

[16] M. Csorba, "Simultaneous localisationa and map building," 1997.

[17] M. W. M. G. Dissanayake, P. Newman, S. Clark, H. F. Durrant-Whyte, and M. Csorba, "A solution to the simultaneous localization and map building (slam) problem," *IEEE Transactions on Robotics and Automation*, vol. 17, pp. 229–241, Jun 2001.

[18] T. Bailey and H. Durrant-Whyte, "Simultaneous localization and mapping (slam): part ii," *IEEE Robotics Automation Magazine*, vol. 13, pp. 108–117, Sept 2006.

[19] R. Smith, M. Self, and P. Cheeseman, "Autonomous robot vehicles," ch. Estimating Uncertain Spatial Relationships in Robotics, pp. 167–193, New York, NY, USA: Springer-Verlag New York, Inc., 1990.

[20] M. Kaess, A. Ranganathan, and F. Dellaert, "iSAM: Incremental smoothing and mapping," *IEEE Trans. on Robotics (TRO)*, vol. 24, pp. 1365–1378, Dec. 2008.

[21] S. Huang and G. Dissanayake, "A critique of current developments in simultaneous localization and mapping," *International Journal of Advanced Robotic Systems*, vol. 13, no. 5, p. 1729881416669482, 2016.

[22] A. Howard, "Real-time stereo visual odometry for autonomous ground vehicles," pp. 3946 – 3952, 10 2008.

[23] C. Harris and M. Stephens, "A combined corner and edge detector," p. 50, 01 1988.

[24] E. Rosten and T. Drummond, "Machine learning for high-speed corner detection," in *Computer Vision – ECCV 2006*, (Berlin, Heidelberg), pp. 430–443, Springer Berlin Heidelberg, 2006.

[25] D. Lowe, "Object recognition from local scale-invariant features," vol. 2, pp. 1150 – 1157 vol.2, 02 1999.

[26] "fovis." http://fovis.github.io/. Accessed: 04-02-2018.

[27] P. H. M. K. D. M. D. F. Albert S. Huang, Abraham Bachrach and N. Roy, "Visual odometry and mapping for autonomous flight using an rgb-d camera," *Int. Symposium on Robotics Research (ISRR)*, August 2011.

[28] P. Besl and N. D. McKay, "A method for registration of 3-d shapes," vol. 14, pp. 239–256, 04 1992.

[29] J. Elseberg, S. Magnenat, R. Siegwart, and A. Nuchter, "Comparison on nearest-neigbour-search strategies and implementations for efficient shape registration," vol. 3, pp. 2–12, 01 2012.

[30] S. Rusinkiewicz and M. Levoy, "Efficient variants of the icp algorithm," in *Proceedings Third International Conference on 3-D Digital Imaging and Modeling*, pp. 145–152, 2001.

[31] S. Nobili, R. Scona, M. Caravagna, and M. Fallon, "Overlap-based icp tuning for robust localization of a humanoid robot," in *2017 IEEE International Conference on Robotics and Automation (ICRA)*, pp. 4721–4728, May 2017.

[32] W. E. Lorensen and H. E. Cline, "Marching cubes: A high resolution 3d surface construction algorithm," in *ACM siggraph computer graphics*, vol. 21, pp. 163–169, ACM, 1987.

[33] B. Curless and M. Levoy, "A volumetric method for building complex models from range images," vol. 3, 09 1999.

[34] R. A. Newcombe, S. J. Lovegrove, and A. J. Davison, "Dtam: Dense tracking and mapping in real-time," in *Computer Vision (ICCV), 2011 IEEE International Conference on*, pp. 2320–2327, IEEE, 2011.

[35] T. Whelan, M. Kaess, M. Fallon, H. Johannsson, J. Leonard, and J. McDonald, "Kintinuous: Spatially extended kinectfusion," 2012.

[36] M. Tanner, P. Piniés, L. M. Paz, and P. Newman, "BOR2G: Building Optimal Regularised Reconstructions with GPUs (in cubes)," in *International Conference on Field and Service Robotics (FSR)*, (Toronto, ON, Canada), June 2015.

[37] M. Nießner, M. Zollhöfer, S. Izadi, and M. Stamminger, "Real-time 3d reconstruction at scale using voxel hashing," *ACM Transactions on Graphics (ToG)*, vol. 32, no. 6, p. 169, 2013.

[38] M. Tanner, P. Pinies, L. M. Paz, and P. Newman, "Denser cities: A system for dense efficient reconstructions of cities," *arXiv preprint arXiv:1604.03734*, 2016.

[39] M. Achtelik, A. Bachrach, R. He, S. Prentice, and N. Roy, "Stereo vision and laser odometry for autonomous helicopters in gps-denied indoor environments," in *Unmanned Systems Technology XI*, vol. 7332, p. 733219, International Society for Optics and Photonics, 2009.

[40] Clearpath Robotics, "Husky a200," 2018.

[41] V. Usenko, J. Engel, J. Stückler, and D. Cremers, "Direct visual-inertial odometry with stereo cameras," in *Robotics and Automation (ICRA), 2016 IEEE International Conference on*, pp. 1885–1892, IEEE, 2016.

[42] S. Nobili, G. Tinchev, and M. Fallon, "Predicting alignment risk to prevent localization failure," *IEEE International Conference on Robotics and Automation*, 2018.

[43] Y. Latif, C. Cadena, and J. Neira, "Robust loop closing over time," 2013.

[44] `https://www.youtube.com/watch?v=y64jsf2ICPY&`. Accessed: 2018-05-02.

[45] J. M. Coughlan and A. L. Yuille, "Manhattan world: Compass direction from a single image by bayesian inference," in *Computer Vision, 1999. The Proceedings of the Seventh IEEE International Conference on*, vol. 2, pp. 941–947, IEEE, 1999.

[46] M. Li, P. Wonka, and L. Nan, "Manhattan-world urban reconstruction from point clouds," in *ECCV*, 2016.